

112272
 7N-90-TM
 (C. CUZZI)
 C10-762

Particle-Gas Dynamics in the Midplane of a Protoplanetary Nebula

JEFFREY N. CUZZI

Ames Research Center, NASA
 E-mail: cuzzi@cloud9.arc.nasa.gov

ANTHONY R. DOBROVOLSKIS

University of California, Santa Cruz

AND

JOELLE M. CHAMPNEY

Applied and Theoretical Mechanics, Inc.

Received March 15, 1993; revised July 7, 1993

In this paper, we study the stage of planetary formation during which the particulate material is still dispersed as centimeter-to-meter sized primordial aggregates. During this stage, particles are able to settle toward the midplane into a layer of mass density comparable to or much greater than that of the gas. Nonlinear, coupled interactions between the particles and the nebula gas become significant and ultimately determine the vertical profiles of the particle density and the mean velocities of the particles and the nearby gas. This is the environment in which the earliest planetesimals probably form. Our numerical models rely on the Reynolds averaged Navier-Stokes equations for the gas and particles and are fully viscous and turbulent (and, for the particles, compressible). Our turbulence modeling uses a Prandtl local shear parametrization, validated by laboratory experiments. We have developed a new model for particle diffusion involving the profile of the nebula gas turbulence and the particle Schmidt number, which is a function of particle size and density. We model a cool, quiescent nebula at 1 AU (280K) and 10 AU (90K) and a higher temperature stage (1000K) at 1 AU.

Our main results include: (a) rapid accretion of planetesimals by gravitationally unstable fragmentation on an orbital time scale (the "Goldreich-Ward instability") is unlikely to occur until objects have already accreted by some other process to the mass of the largest known meteorite samples, if at all; (b) from "seeds" as small as 10 m, growth of 10- to 100-km planetesimals can proceed rapidly by drift-augmented accretion in the particle-rich midplane with orbital decay of about 1% for the growing planetesimals; (c) outward transport of vapor and small entrained chips can account for significant radial compositional and mineralogical

mixing in primitive meteorite parent bodies. Other implications may be drawn concerning particle random collisional velocities and the time scales of midplane turbulence. © 1993 Academic Press, Inc.

1. INTRODUCTION

Over the past decade, a number of theoretical and observational studies have suggested that flattened disks of dust and gas will form as a natural by-product of stellar formation and have established their global thermal and dynamical properties (see, e.g., *Protostars and Planets III* for recent reviews). In broad form, flattened disks of dusty gas result from gravitational collapse of dense regions of interstellar clouds (Cassen *et al.* 1985). Collisional accretion of comet-sized planetesimals within such a disk leads to the growth of dense planetary cores (Safro-nov 1969), followed, at least in the outer Solar System, by hydrodynamical accretion of nebula gas to form jovian-type planets (Mizuno *et al.* 1978). However, poorly understood stages connect these landmark events.

One major area of current uncertainty is the transition from a gas-dominated accretion disk to a disk of comet-sized planetesimals. In this stage, which is the topic of this paper, collective aerodynamic interactions between macroscopic particles and the surrounding gaseous nebula involve complex feedback processes which affect the evolution of the gas and particle phases in different ways. In fluid dynamics, these are known as two-phase fluid systems. In most research to date, this stage has been neglected. Typical protoplanetary nebula models assume that the particle phase is composed of interstellar-sized grains, which are strongly coupled to the gas by drag

Presented at the Planet Formation program held at the Institute for Theoretical Physics of the University of California at Santa Barbara, in Fall 1992.

forces and remain uniformly mixed, merely increasing the density of the gas phase. Since the average mass density of the solids is only 1% or so of the gas density, such solids have little dynamical influence.

Practically all of our tangible evidence of planetesimal accretion is in the form of meteorites with masses less than 10^4 kg, many of which show little or no evidence for metamorphic processes beyond mere compression. Primitive meteorites in this mass range overwhelmingly point to an abundance of constituent building blocks in the 0.01–1-cm size range, although the process by which these constituents (primarily “chondrules” and their mineralogical relatives) are first created and accumulated is not understood. On independent theoretical grounds, it is generally accepted that grain growth leads rapidly (in 10^3 – 10^4 orbit times) from interstellar grain sized to centimeter-sized particles which are assumed to settle to the nebula midplane in tens or hundreds of orbit times (Völk *et al.* 1980, Weidenschilling 1984, Mizuno *et al.* 1988, and Weidenschilling and Cuzzi 1993). This accretion probably proceeds efficiently, with sticking coefficient of order unity, until particles are about 1 m in size and impact cratering or disruption becomes significant (Chokshi *et al.* 1993). Subsequently, collisional accretion and destruction processes could be in rough balance. Weidenschilling (1984) modeled a situation in which extended evolution occurred without significant change in the particle size distribution once accretion had proceeded to this point. In this paper we restrict ourselves to particles smaller than about 1 m in radius.

The dynamical effects of dust–gas segregation were downplayed in early studies which hypothesized a gravitational instability in this settled particle phase (Edgeworth 1949, Safronov 1969, and Goldreich and Ward 1973). Despite several subsequent attacks on this aspect of the problem by Weidenschilling (1980, 1984, 1988), it is still widely assumed in the community that the particle layer quickly becomes gravitationally unstable, leading immediately to a population of comet-sized planetesimals which are sufficiently large to be entirely decoupled from the gas. In this paper, we demonstrate that this is unlikely to occur until particles have grown by binary accretion or by sticking to a sufficient size (meters or larger) that they already contain the mass equivalent of practically all existing primitive meteorite samples.

The quantity triggering gravitational instability is the volume mass density ρ_p of the particulates. The condition for gravitational instability, while formally derived by finding growing modes from a dispersion relation, is equivalent to the condition that the oscillation frequency due to solar gravity be less than that due to local self-gravity (cf. Toomre 1964),

$$\frac{c_p \Omega}{\pi G \sigma_p} \approx \frac{H_p \Omega^2}{\pi G \sigma_p} \approx \frac{\Omega^2}{\pi G \rho_p} < 1, \quad (1)$$

where c_p is the typical random velocity of the particles, Ω is their orbital angular velocity, G is the gravitational constant, $\sigma_p \approx \rho_p H_p$ is surface mass density, and the thickness of the particle layer is $H_p \approx c_p / \Omega$. This reduces to a critical particle volume mass density of $\rho_{p,\text{crit}} \approx \Omega^2 / \pi G \approx M_\odot / \pi r^3$. Other, more detailed treatments provide improved estimates of the *minimum* critical density for an initial *axisymmetric* perturbation (having scale length 8 – $10 H_p$) of $\rho_{p,\text{crit}} \approx 3M_\odot / 2\pi r^3$ (Safronov 1987, 1991) or $\sim 15M_\odot / 8\pi r^3$ (Sekiya 1983). These critical densities can be expressed as 2.0 – $2.5\rho^*$, where the quantity $\rho^* = 3M_\odot / 4\pi r^3$ is the mass of the Sun averaged over a spherical volume with radius equal to the distance of the perturbation from the Sun. Actual *bound fragments* with these length scales require a considerably higher critical density ($\sim 15\rho^*$; Coradini *et al.* 1981, Safronov 1991) to become unstable, which Safronov (1991) suggests might result from an extended evolution which begins with an axisymmetric instability. Further subtleties of gravitational instability are beyond the scope of this paper; for our purposes, we adopt the critical density criterion $\rho_{p,\text{crit}} = 2\rho^*$ of Safronov (1991) noted above as a necessary condition for *any* gravitational instability. This criterion may be used by itself or to estimate a vertical thickness $H_p \approx \sigma_p / \rho_{p,\text{crit}}$. At 1 AU from the protosun, for example, where the usual “minimum mass nebula” assumption gives $\sigma_p \approx 10 \text{ g cm}^{-2}$, incipient gravitational instability requires $H_p \lesssim 10^3 \text{ km}$, associated with particle random velocities $c_p \approx H_p \Omega < 20 \text{ cm sec}^{-1}$. The more dramatic Goldreich–Ward *fragmentation* scenario requires layer thicknesses and random velocities that are at least an order of magnitude smaller.

Because the gas-rich envelope of the protoplanetary nebula is partly supported by an internal pressure gradient (Weidenschilling 1977, and Section 2.1 below), its orbital speed at 1 AU is 50 – 100 m sec^{-1} slower than that of the particle-dominated layer (at a nebula temperature of roughly 300 K). Fractionally this is less than 1%. However, in a region near the midplane where settling of particulates has brought their mass density to a value approaching or exceeding that of the gas, drag forces accelerate the entrained gas nearly to Keplerian velocity. This velocity difference generates a turbulent shear zone between the particle-dominated layer and the gas-dominated regions above and below, with turbulent speeds on the order of several meters per second. Turbulent and dynamical time scales in the boundary layer are much longer than the stopping times t_s of millimeter-to-centimeter scale particles due to aerodynamic drag. Consequently the dispersion velocity c_p of such particles is also excited to a value of several meters per second, comparable to that of the gas fluctuations and sufficient to prevent further settling (Weidenschilling 1980, Coradini *et al.* 1980). Using such scaling arguments, Weidenschilling (1980) estimated a minimum thickness of the particle layer H_p which was about an order of magnitude too large for the Gold-

reich–Ward instability (GWI) to occur. Although this very severe problem has been known for over a decade and duly noted in recent reviews (Weidenschilling 1988, Weidenschilling *et al.* 1989, Wetherill 1990), it has not been thoroughly appreciated in the broad community (e.g., Sekiya and Nakagawa 1988, Wasson and Kallemeyn 1988, Haack *et al.* 1990, Barge and Pellat 1991, Ruden and Pollack 1991, Kolvoord and Greenberg 1992, Watanabe and Miyama 1992, Grimm and McSween 1993). In this paper, we present detailed numerical calculations as further evidence that gravitational instability does not occur as originally suggested in disks of centimeter-scale particles, and demonstrate that it will not occur even for orders of magnitude more massive particles between 10 cm and 1 m in radius.

The most detailed recent study of gas–particle interactions in the nebula, by Nakagawa *et al.* (1986), obtains the particle and gas densities and velocities analytically in a two-phase nebula under certain simplifying assumptions. They demonstrate how the headwind between the particles and the surrounding pressure-supported gas (Whipple 1972, Adachi *et al.* 1976, Weidenschilling 1977) diminishes in a dust-dominated central layer, where the mass-dominant particles drive the intermingled gas to velocities approaching Keplerian. However, their nebula is assumed to be inviscid (i.e., laminar or nonturbulent) which is internally inconsistent; as noted above, the steep vertical gradient in the orbital velocity, between the gas entrained within the particle layer and that in the overlying pressure-supported region of the nebula, is capable of generating a turbulent viscosity in and of itself, which will alter the particle vertical distribution (Weidenschilling 1980). Consequently, the particle density distribution cannot be constrained by the Nakagawa *et al.* model. Despite this inconsistency, for a *given* particle vertical distribution, the Nakagawa *et al.* model does a fair job of roughly predicting the mean flows of the two phases, and is being used as part of some ongoing particle accretion modeling (e.g., Weidenschilling and Cuzzi 1993). In this paper, we present a fully viscous model suitable for further studies of the final stages of settling and particle accretion in which planetesimal formation must occur.

We have assumed that there is no other source of turbulence during the stages we model. Various mechanisms for inducing global nebula turbulence have been widely discussed but remain controversial. Elmegreen (1978, 1979) suggested that stellar wind flows across the face of the nebula induce turbulence. Lin and Papaloizou (1980) suggested that thermal convection drives nebula turbulence. Prinn (1990) suggested that mismatches between infall and orbital velocities generate turbulence. Observations of T Tauri stars show that the “active” or classical T Tauri (CTT) stage of disk evolution is characterized by strong winds and high thermal luminosity such as might characterize a large global turbulent viscosity; however,

this stage seems to last only a few million years. Currently accepted values of nebula kinematic viscosity in the CTT stage are on the order of 10^{13} – 10^{15} cm² sec^{−1}, several orders of magnitude larger than values we will present here. In addition, brief but energetic “FU Orionis” phases are believed to punctuate the CTT stage (Hartmann *et al.* 1993); in these stages a considerable fraction of the circumstellar disk and its particulates, at least out to 1 AU, may be heated to 1000 K or more. “Weak-line” T Tauri (WTT) systems have a much lower particulate opacity, possibly due to accumulation of microscopic dust into larger particles such as studied here (Cuzzi and Weidenschilling 1992, Miyake and Nakagawa 1992, 1993), and show no evidence for significant global viscosity. More of these systems seem slightly older than comparable numbers of CTT systems—possibly ranging into the 10⁷-year stage tentatively indicated in the range of meteorite accumulation ages (Swindle and Podosek 1988). Note that there is no evidence that either the nebula gas or the particulates have been *removed* by this time—merely that the particulate opacity and overall luminosity have diminished greatly.

One certainly expects that there will be a stage during which the opacity and turbulence in the protoplanetary disk decrease, probably that during which most of the particle accumulation occurs. It may even be that particle growth *causes* cessation of strong convection and the associated large turbulent viscosity by diminishing the Rosseland mean opacity and its temperature dependence below critical threshold values (Cuzzi and Weidenschilling 1992). This may or may not be what is known as the weak line T Tauri stage. In the present paper we focus on parameters which are appropriate for such a low global viscosity, post-CTT stage. In any case, our assumption of zero global turbulence provides the most conservative possible situation for preventing particulate layers from undergoing gravitational instability; any global turbulence would add to the self-consistent shear turbulence we calculate, further enhancing vertical diffusion of the particles, and occurrence of the GWI would be even more strongly precluded. We return to these implications in Section 5.

The extensive array of symbols used in this paper is summarized in Appendix C. In Section 2, we discuss our method of solution; some readers may wish to skip this section initially. Many of the critical details are contained in Appendices A and B. Section 2.1 summarizes our fundamental equations. Appendix A derives these equations, while discussing some of the critical subtleties involved in merely obtaining a proper set of two-phase fluid equations to solve. The primitive equations governing both gas and particle phases must be averaged in some way to remove the unknown fluctuating density and velocity components. This process generates *correlation terms* of two types: products of velocity fluctuations alone and

products of both velocity and density fluctuations. Section 2.2 shows how we model the velocity-velocity correlations physically, in terms of the gas turbulent viscosity and turbulent kinetic energy. In Section 2.3 we present our approach to modeling the density-velocity correlations, which leads to a diffusion equation for particles in the turbulence. In Section 2.4 we quickly summarize some details of our numerical procedure. In Section 3 we present the parametrized nebula physical model we adopt, while Section 4 presents our results for a variety of nebula environments. Those more interested in results than in our methodology and the basic fluid dynamics may wish to begin with Section 3 or 4. In Section 5, we discuss some interesting implications of our work for planetesimal growth and mineralogical mixing. We summarize our conclusions in Section 6.

2. SOLUTION TECHNIQUE

2.1. Equations of Motion

The continuity and momentum equations for each phase must be solved simultaneously. The equations are formulated and solved in cylindrical geometry. The equations are expanded in detail in Appendix A; our coordinate and velocity system is (r, θ, z, u, v, w) for both gas and particles. Azimuthal symmetry ($\partial/\partial\theta = 0$) is assumed, and radial variation is demonstrably smaller than vertical variation in all dependent variables ($\partial/\partial r \ll \partial/\partial z$). This leads naturally to a 1-D (vertical) solution space. The gas density is very nearly constant (see below); the continuity equation for the particle density is of the form

$$\frac{\partial}{\partial t} \rho_p + \nabla \cdot (\rho_p \mathbf{v}_p) = 0, \quad (2)$$

where \mathbf{v}_p is the particle vector velocity and ρ_p is the particle volume mass density.

The momentum equations may be expressed in the general form

$$\begin{aligned} \frac{\partial}{\partial t} (\rho \mathbf{v}) + \rho (\mathbf{v} \cdot \nabla) \mathbf{v} + \mathbf{v} \nabla \cdot (\rho \mathbf{v}) = & -\nabla P - \rho \nabla \Phi \\ & \pm \rho_p (\mathbf{v}_p - \mathbf{v}_g)/t_s. \end{aligned} \quad (3)$$

Equations (3) above are just the Navier-Stokes equations in conservative form, including pressure, gravity, and gas drag terms, respectively, on the right-hand side. In these equations, the velocities are in an inertial frame, and Φ is the gravitational potential from the Sun. For the gas phase, P is simply the thermodynamic pressure and the upper sign is chosen in the gas drag (last) term; for the particle phase $P = 0$ while the lower sign is chosen in

the drag term. In either case, t_s is the stopping time of the particles in the gas, which is inversely proportional to their drag coefficient (Weidenschilling 1977; see Section 2.3.2). Transport terms due to molecular viscosity have been neglected, as turbulent viscosity dominates. In several instances below, we will make use of the fact that our goal is a time-invariant, steady-state solution.

As described in Appendix A, the primitive equations are treated by separating the particle density and all velocity components into mean and fluctuating parts:

$$\mathbf{v}_g = \bar{\mathbf{v}}_g + \mathbf{v}'_g; \quad \mathbf{v}_p = \bar{\mathbf{v}}_p + \mathbf{v}'_p; \quad \rho_p = \bar{\rho}_p + \rho'_p. \quad (4)$$

The equations are expanded out and time averaged (Reynolds averaged) as described in Appendix A; products involving only one fluctuating quantity time average to zero, but products of fluctuating quantities cannot be assumed to do so. These correlations are modeled as described in the following sections.

The resulting system proves to be “stiff,” or difficult to solve numerically, because the mean gas and particle velocities are dominated by their azimuthal components. Vertical and radial drift velocities can be as small as a few centimeters per second compared to orbital speeds of tens of kilometers per second. This large dynamic range led us to a perturbation approach; accordingly we further expanded the mean azimuthal velocities as

$$\bar{v}_g = v_0 + v_g^*, \quad \bar{v}_p = v_K + v_p^*, \quad (5)$$

where

$$v_K = \sqrt{GM/r} \quad (6)$$

is the Keplerian speed of a free particle orbiting the Sun at a radius r , and the orbital velocity of the gas including its pressure gradient is

$$v_0 = (1 - \eta)v_K. \quad (7)$$

Here,

$$\eta \equiv -\frac{r}{2\rho_g v_K^2} \frac{\partial P}{\partial r} \approx 10^{-3} \quad (8)$$

after Adachi *et al.* (1976; see also Nakagawa *et al.* 1986, but note misprint in their Eq. (1.9)). That is, our unperturbed state has the particles in Keplerian rotation (at the equator) and the gas rotating slightly slower due to pressure support with its radial pressure gradient parametrized by η .

This choice of a basic state simplifies the equations of motion (Eqs. (A11)–(A13) of Appendix A) considerably,

because the largest terms $-\bar{\rho}GM/r/R^3$ and $\bar{\rho}\bar{v}^2/r$ in Eq. (A11) nearly cancel. Several other terms can also be neglected by scaling. For example, $\bar{\rho}\bar{u}(\partial/\partial r)\bar{v}$ is negligible compared with $\bar{\rho}\bar{w}(\partial/\partial z)\bar{v}$, while azimuthal derivatives $\partial/\partial\theta$ are neglected by the assumption of rotational symmetry. For the particle phase, $P = 0$ and $(\partial/\partial t)\bar{\rho}'\bar{v}'$ is neglected relative to $\bar{\rho}(\partial/\partial t)\bar{v}$, so that the momentum Eqs. (A11)–(A13) become

$$\begin{aligned} \bar{\rho}_p \frac{\partial}{\partial t} \bar{u}_p + \bar{\rho}_p \bar{w}_p \frac{\partial}{\partial z} \bar{u}_p &= 2(\bar{\rho}_p v_p^* + \overline{\rho'_p v'_p}) v_K / r \\ &- \frac{\partial}{\partial z} (\bar{\rho}_p \overline{u'_p w'_p}) - \frac{\partial}{\partial z} (\bar{\rho}'_p \overline{u'_p w'_p}) - \bar{\rho}'_p \bar{w}'_p \frac{\partial}{\partial z} \bar{u}_p \\ &- \bar{\rho}_p (\bar{u}_p - \bar{u}_g) / t_s, \end{aligned} \quad (9)$$

$$\begin{aligned} \bar{\rho}_p \frac{\partial}{\partial t} v_p^* + \bar{\rho}_p \bar{w}_p \frac{\partial}{\partial z} v_p^* &= -\frac{1}{2}(\bar{\rho}_p \bar{u}_p + \overline{\rho'_p u'_p}) v_K / r \\ &- \frac{\partial}{\partial z} (\bar{\rho}_p \overline{v'_p w'_p}) - \frac{\partial}{\partial z} (\bar{\rho}'_p \overline{v'_p w'_p}) - \bar{\rho}'_p \bar{w}'_p \frac{\partial}{\partial z} v_p^* \\ &- \bar{\rho}_p (\eta v_K + v_p^* - v_g^*) / t_s, \end{aligned} \quad (10)$$

$$\begin{aligned} \frac{\partial}{\partial t} (\bar{\rho}_p \bar{w}_p) + \frac{\partial}{\partial z} (\bar{\rho}_p \bar{w}_p^2) &= -\bar{\rho}_p GMz / r^3 \\ &- \frac{\partial}{\partial z} (\bar{\rho}_p \overline{w'_p w'_p}) - 2 \frac{\partial}{\partial z} (\bar{\rho}'_p \overline{w'_p w'_p}) - \bar{\rho}_p \bar{w}_p / t_s. \end{aligned} \quad (11)$$

By the same token, the particle continuity Eq. (A7) reduces to

$$\frac{\partial}{\partial t} \bar{\rho}_p + \frac{\partial}{\partial z} (\bar{\rho}_p \bar{w}_p + \overline{\rho'_p w'_p}) = 0. \quad (12)$$

The equations of motion for the gas are even simpler. Because our region of interest is significantly thinner than the gas vertical scale height, and because bulk gas motions are far slower than the sound speed, the gas is treated as incompressible at a constant density. That is, we assume $\rho'_g = 0 = \bar{w}_g$. Therefore we do not solve the equation of vertical momentum (A13) for the gas, while the gas continuity Eq. (A7) reduces to

$$\frac{\partial}{\partial t} \bar{\rho}_g = 0. \quad (13)$$

For the gas, the central force gravity, centrifugal, and pressure gradient terms nearly cancel and, as in the particle equations, we drop demonstrably small terms to leave

$$\bar{\rho}_g \frac{\partial}{\partial t} \bar{u}_g = 2\bar{\rho}_g v_0 \bar{u}_g / r - \frac{\partial}{\partial z} (\bar{\rho}_g \overline{u'_g w'_g}) + \bar{\rho}_p (\bar{u}_p - \bar{u}_g) / t_s, \quad (14)$$

$$\begin{aligned} \bar{\rho}_g \frac{\partial}{\partial t} v_g^* &= -\frac{1}{2} \bar{\rho}_g v_0 \bar{u}_g / r - \frac{\partial}{\partial z} (\bar{\rho}_g \overline{v'_g w'_g}) \\ &+ \bar{\rho}_p (\eta v_K + v_p^* - v_g^*) / t_s. \end{aligned} \quad (15)$$

2.2. Modeling Shear-Driven Turbulence

Above and in Appendix A, we have described how we arrive at the equation set, which contains a variety of terms relating the mean quantities of interest by time averages of unknown fluctuating quantities. In the next few subsections, we describe our procedure for modeling these time-averaged correlation terms. The first part of this modeling will be familiar (Schlichting 1969). In a technique originally due to Boussinesq, the gas velocity correlations (Reynolds stresses) are expressed in terms of a scalar kinematic eddy viscosity ν_T , a scalar turbulent kinetic energy per unit mass $k \equiv (\overline{u'_g u'_g} + \overline{v'_g v'_g} + \overline{w'_g w'_g})/2$, and gradients of the mean velocity:

$$\begin{aligned} \overline{u'_g u'_g} &= \frac{2}{3} k, \quad \overline{v'_g w'_g} = -\nu_T \frac{\partial \bar{v}_g}{\partial z}, \\ \overline{v'_g v'_g} &= \frac{2}{3} k, \quad \overline{u'_g w'_g} = -\nu_T \frac{\partial \bar{u}_g}{\partial z}, \\ \overline{w'_g w'_g} &= \frac{2}{3} k, \quad \overline{u'_g v'_g} = 0. \end{aligned} \quad (16)$$

In the above equations, we have used scaling relationships to eliminate the (small) terms in $\partial/\partial r$, as noted previously. Models of ν_T and k are described below. Comparable *particle* velocity correlation terms occur in the particle momentum equation, which may be related to k and ν_T as discussed in more detail in Section 2.3 and in Appendix B. Note that the formula for the Reynolds stresses in Champney and Cuzzi (1990) is misprinted; the factor $(\rho_0 + \rho)$ in their equation (33) should be inside the brackets. The correct expression is equivalent to those given above.

2.2.1. Turbulent viscosity. It is important to point out the difference between turbulence caused by thermal convection (Lin and Papaloizou 1980, Coradini *et al.* 1980, Ruden and Lin 1986, Cabot and Pollack 1992) and the shear-driven turbulence which concerns us herein. The essential difference lies in the fact that shear-driven turbulence derives its energy from the *local* mean flow and has intrinsic length and time scales, whereas thermal convection derives its energy from the *global* mean flow and has length and time scales that depend on the entire energy budget of the flow as well as on specific details of the geometry. Since the energy budget depends on the structure of the turbulence itself, convective turbulence is a highly nonlinear and poorly characterized phenomenon (e.g., Cabot *et al.* 1987a,b, 1990). Additional difficulties

may arise in strongly, and/or systematically, perturbed systems in which the correlation terms $\overline{v_i'v_j'}$ may result in negative or nonscalar “viscosities” (Borderies *et al.* 1983, Cabot *et al.* 1987a,b, 1990, Prinn 1990, Cabot and Pollack 1992). For example, in convective turbulence, where the large or *integral* scales are on the order of a gas scale height in size, rotational anisotropy can be an important factor (Cabot *et al.* 1987a,b). Although no form of turbulence is really well understood, shear-driven turbulence is fairly well constrained in comparison (Tennekes and Lumley 1972), and a variety of parametrizations provide satisfactory representations of real shear flows of many sorts (see, e.g., Schlichting 1969, Rodi 1980, Coakley 1987).

Models of turbulent systems often rely on dimensional arguments which lead to turbulent viscosities expressed in scaled form as

$$\nu_T = \alpha UL, \quad (17)$$

where U and L are the characteristic velocity and length scales, and α is a dimensionless coefficient. If U is taken to be the sound speed and L the scale height, various current nebula models favor α in the poorly constrained range 10^{-2} and 10^{-4} on the scale of a disk scale height (Cabot *et al.* 1987a,b; see Weidenschilling 1988 and Weidenschilling and Cuzzi 1993 for recent reviews). These values are much smaller than those adopted even in the recent past (e.g., Mizuno *et al.* 1988, Morfill and Völk 1984).

More complex parametrizations of turbulent shear flow include not only dimensional approaches such as the α -models, but also (a) experimentally validated but less widely used (in the astrophysics community) parametric zero-equation or Prandtl models, (b) one- or k -equation models (where k is the turbulent kinetic energy per unit mass), and (c) two-equation or $k - \epsilon$ models, where ϵ is the dissipation rate of k . All relate the turbulent velocity fluctuations (and the associated turbulent viscosity) to the mean *local* properties of the flow. The latter two incorporate advective and diffusive transport of k by the flow itself. We shall see that the specifics of the solution are sensitive to the various constants involved. In what follows we make as clear as possible the way in which the constants enter into the solution.

A simple estimate of the turbulent viscosity in the boundary layer is obtained as follows. A nonturbulent flow may be associated with a Reynolds number

$$\text{Re} = \frac{UL}{\nu_m}, \quad (18)$$

where ν_m is the molecular kinematic viscosity of the fluid. It is well known that laminar flow persists while Re is

increased until turbulence sets in at some critical value of $\text{Re} = \text{Re}^*$, where the critical Reynolds number Re^* depends on the flow geometry. For larger Re , eddy motions generate a turbulent viscosity

$$\nu_T \approx \frac{UL}{\text{Re}^*} = \frac{\text{Re}}{\text{Re}^*} \nu_m, \quad (19)$$

such that the effective Reynolds number (UL/ν_T) remains fixed at Re^* . In a thin shear flow such as the environment under study here, U may be taken as the total velocity differential across the turbulent boundary layer between the Keplerian particles and the pressure-supported gas, $\Delta V = v_K - v_0 \approx 10^{-3} v_K$ (Sections 2.1 and 3). In what follows we need to distinguish between several different length scales. Our situation is a somewhat novel blend of a classic “Ekman” regime, in which the orbital rotation frequency dominates the overall boundary layer thickness, and a normal nonrotating boundary layer regime in which the local transport length and time scales are independent of the orbit frequency. Because the vertical profiles of gas velocity closely resemble those seen in the Ekman regime, we adopt as our benchmark vertical length scale the e -folding thickness of the turbulent Ekman layer L_E in the rotating system, which itself depends on ν_T as

$$L_E \equiv (\nu_T/\Omega)^{1/2} \quad (20)$$

(Schlichting 1969, Hinze 1975, Goldreich and Ward 1973, Dobrovolskis 1983). A generic length scale $L = c_L L_E$ will be used in all derivatives for scaling purposes, where c_L is of order unity. Detailed engineering fluid dynamics formulations, of which we will be making considerable use, more commonly utilize the specific 1% boundary layer depth δ , the distance at which the mean flow velocity differs by only 1% from its free stream value. From the definition of the Ekman depth L_E , $\delta = c_\delta L_E$, where $c_\delta > c_L$. Substituting ΔV for U and $c_L L_E$ for L into Eq. (19) then gives

$$\nu_T \approx \frac{c_L \Delta V (\nu_T/\Omega)^{1/2}}{\text{Re}^*}$$

or

$$\nu_T \approx \frac{c_L^2 \Delta V^2}{\Omega \text{Re}^{*2}}. \quad (21)$$

A better turbulence model relates turbulence to the local velocity shear, such as originally due to Prandtl (Schlichting 1969, Rodi 1980, Coakley 1987), which may be written in the form

$$\nu_T = \ell^2 S, \quad (22)$$

where S is a measure of the shear, and ℓ is a characteristic length scale of the problem, called the mixing length.

For this vertical boundary layer problem, we take ℓ as proportional to the boundary layer depth δ and take S as the vertical gradient of the horizontal velocity:

$$\ell = c_\nu \delta, \quad S = \left| \frac{\partial V}{\partial z} \right|. \quad (23)$$

Then the turbulent viscosity from (22) becomes

$$\nu_T = c_\nu^2 \delta^2 \left| \frac{\partial V}{\partial z} \right|. \quad (24)$$

Using these definitions, laboratory measurements in jet boundary layer geometries show that $c_\nu = 0.045$ (Coakley 1987), as long as the system is negligibly affected by rotation;

$$\text{Rossby number } \text{Ro} \equiv \frac{U}{\Omega L} \gg 1. \quad (25)$$

Below we show this to be the case. Values of $c_\nu = 0.1$ provide better fits to observations in slightly different flow geometries such as wake, shear, or wall-bounded flow (Coakley 1987, Rodi 1980). In practice, we employ the Prandtl model in the form of Eq. (24), with the velocity gradient determined locally, and continuously adjust δ to be the actual height at which the perturbed gas velocity becomes 1% of its maximum value. We have found that this implies c_δ is approximately 2.5 and then use this value to obtain related quantities of interest.

For instance, scaling may be used to obtain a value for Re^* . Solving for ν_T by approximating the derivative in Eq. (24) as a ratio of characteristic velocity and length scales, and using $c_L L_E$ as the appropriate length scale L , gives

$$\nu_T \approx (c_\nu \delta)^2 \frac{\Delta V}{L} = \frac{c_\delta^4 c_\nu^4 \Delta V^2}{c_L^2 \Omega}. \quad (26)$$

Comparing this to Eq. (21) for ν_T in terms of the critical Reynolds number Re^* , we find that (for $c_\delta = 2.5$, $c_\nu = 0.05 - 0.1$ and $c_L = 1.5$)

$$\text{Re}^* = c_L^2 c_\delta^{-2} c_\nu^{-2} \approx 45 - 180. \quad (27)$$

The depth of the 1% shear layer is then $\delta = (c_\delta^3 c_\nu^2 / c_L) (\Delta V / \Omega)$, and the generic scale $L = c_L L_E \approx c_L \Delta V / \Omega \text{Re}^*$. These values are only about 10^{-4} of the radius in the nebula,

small compared to a typical vertical scale height of the nebula gas ($\sim 10^{-1}$ of the radius).

This scaling also indicates that our situation is probably never dominated by rotation; the Rossby number (using $L = c_L L_E$, and Eqs. (20) and (27)) is

$$\text{Ro} = \frac{\Delta V}{c_L L_E \Omega} = \frac{\Delta V L_E}{c_L \nu_T} = \frac{\text{Re}^*}{c_L^2} = c_\delta^{-2} c_\nu^{-2} \approx 20 - 80. \quad (28)$$

The large Rossby number implies that rotation is unimportant in determining the *local* structure of the turbulence; therefore, the turbulence should be fairly isotropic and the Prandtl parametrization with $c_\nu \approx 0.05$ to 0.1 should be satisfactory. On the other hand, the overall vertical profile is limited by the nebula rotation frequency (Section 2.2.2). In our numerical modeling, Re^* plays a subsidiary role; rather we adopt a value for the experimentally determined constant c_ν . The qualitative nature of the solutions does not depend sensitively on the value of c_ν .

Note that the Prandtl model assumes the turbulence is locally generated and damped—that is, turbulence exists only where velocity gradients exist. Strictly, the Richardson number criterion allows turbulence to exist only when

$$\text{Ri} \equiv \frac{g}{T} \left(\frac{\partial T}{\partial z} + \frac{g}{c_p} \right) \left(\frac{\partial v}{\partial z} \right)^{-2} < 0.20 - 0.25, \quad (29)$$

where $g = z \Omega^2$ is the local vertical acceleration of gravity, c_p is the heat capacity of the gas at constant pressure, and g/c_p is the adiabatic lapse rate (Tennekes and Lumley 1972, Goldreich and Ward 1973). Order-of-magnitude scaling arguments using typical velocity gradients from our model results confirm that the Richardson number criterion is always satisfied on the average in our models, as has been found by previous workers (Goldreich and Ward 1973, Weidenschilling 1980). However, *very* near the midplane ($z \ll \delta$), vertical gradients vanish by symmetry. This might cause the critical Richardson number criterion of Eq. (29) to be violated locally, implying that turbulence could also vanish near the midplane (Safronov 1991, 1992).

This concern is diminished or removed by consideration of the next level of sophistication in turbulence modeling, which includes transport of turbulence by the turbulent process itself. As mentioned above, state-of-the-art turbulence modeling deals with self-consistent generation, transport, and damping of turbulence using more complex one- or two-equation models. In these models, turbulent viscosity is related to turbulent kinetic energy k , and its dissipation rate ε , as described below. Champney and Cuzzi (1990) experimented with a two-equation or k - ε model. The k - ε model calculations in Champney and Cuzzi (1990; see also Cuzzi *et al.* 1989) show that the

turbulence diffuses itself into the midplane region where the mean velocity shear, and the Prandtl model turbulence, would approach zero. Simple scaling arguments in support of this are presented in Section 2.2.2 below. Although Champney and Cuzzi (1990) found poor quantitative agreement between the k - ε and the simpler Prandtl model, they had assumed $\text{Re}^* = 500$ (also adopted by Goldreich and Ward 1973), which is probably too large; a smaller value of Re^* would improve the agreement. In this paper, we use a Prandtl model but modify it slightly to be consistent with the behavior we expect from the more sophisticated models. To do this, we have generally adjusted our turbulent kinetic energy (and eddy viscosity) profiles to be uniform below the maximum shear region where the turbulence is generated. This is discussed in the next section. In Section 4 we also present sensitivity studies which show this simplification to have little effect.

2.2.2. Turbulent kinetic energy and its relationship to viscosity. Turbulent kinetic energy terms (e.g., $\overline{u'u'} \approx \overline{v'v'} \approx \overline{w'w'} \approx 2k/3$) play a prominent role in the particle momentum and continuity equations (Appendix A and Eqs. (9)–(12)). There are several paths to modeling the turbulent kinetic energy. We begin from the fact that in isotropic turbulence the off-diagonal elements of the stress or pressure tensor are a certain fraction of the on-diagonal elements in magnitude. That is, $\overline{V'_i V'_j} \approx c_k \overline{V'_i V'_i}$, where $\overline{V'_i V'_i}$ is a single element and $c_k \approx 0.4$ (Tennekes and Lumley 1972, p. 50). This then leads to

$$k = \frac{1}{2} (\overline{u'u'} + \overline{v'v'} + \overline{w'w'}) \approx \frac{3}{2c_k} \overline{u'v'} = \frac{3}{2c_k} \nu_T \left| \frac{dV}{dz} \right|, \quad (30)$$

where we have used Eq. (16), and $|dV/dz|$ is the vertical derivative of the total velocity. Basically this is our parametrization for k .

To model particle diffusion, we need a model of the eddy frequencies (Section 2.3 and Appendix B). This results from an understanding of the energetics of the turbulence. A common approximation is made that turbulence is in a local production–dissipation equilibrium; using a typical expression for the local production rate \mathcal{P} of k (Rodi 1980, Eqs. (2.34), (2.48), (2.60); Hinze 1975), this approximation yields

$$\varepsilon = \mathcal{P} \approx \nu_T \left(\frac{\partial V}{\partial z} \right)^2, \quad (31)$$

where ε is the dissipation rate of the turbulent kinetic energy k . Combining Eqs. (30) and (31) yields the Kolmogorov–Prandtl formula

$$\nu_T = c_\mu k^2 / \varepsilon, \quad (32)$$

where $c_\mu = 4c_k^2/9 \approx 0.09$ (Rodi 1980). We obtain an expression for the dissipation rate ε by rewriting Eq. (31) in the form

$$\varepsilon = \nu_T \left| \frac{dV}{dz} \right| \left| \frac{dV}{dz} \right| = \nu_T \left| \frac{dV}{dz} \right| \omega = c_\mu^{1/2} k \omega = c_\mu^{1/2} \text{Ro} \Omega k, \quad (33)$$

where we have used Eq. (30) and defined the mean field vorticity $\omega = |dV/dz| = |\Delta V/L| = \text{Ro} \Omega$. By definition of k and ε , the time scale for dissipation of k is $T_\varepsilon = k/\varepsilon = (c_\mu^{1/2} \text{Ro} \Omega)^{-1}$. Turbulence folklore holds that the (large) energy-containing eddies lose a significant fraction of their energy in a turnover time (Tennekes and Lumley 1972, p. 21); that is, $T_\varepsilon \approx 2\pi/\Omega_e$, where Ω_e is the large eddy turnover frequency. Thus,

$$\Omega_e \approx \frac{2\pi}{T_\varepsilon} = 2\pi c_\mu^{1/2} \omega = 2\pi c_\mu^{1/2} \text{Ro} \Omega \approx 2\text{Ro} \Omega \approx 40\Omega - 160\Omega. \quad (34)$$

Although the factor of two is somewhat uncertain in the above expression for Ω_e , this relationship provides us with an important new insight into the environment of interest. Specifically, in the case where the particles have settled into such a thin layer that the vertical scale is comparable to L_E , the large eddy turnover frequency is more than an order of magnitude faster than the orbital frequency. By way of contrast, most workers in the field (following Safronov 1969 and Völk *et al.* 1980) assume that the turnover frequency of the large (*outer* or *integral*) scale eddies, Ω_e , is comparable to the local rotation frequency Ω in the nebula. This assumption may be satisfactory for modeling convective turbulence with vertical length scales comparable to the gas scale height. In fact, recent computational simulations verify its validity in the general case where the rotation alone provides the driving mechanism (Coleman *et al.* 1990, 1992). However, we believe Eq. (34) is more appropriate for our thinner, shear-driven boundary layers. This is a result of our somewhat mixed regime: the turbulent boundary layer is fundamentally driven by the imposed *velocity* difference ηV_K , but the gas can only sustain a vertical *length scale* constrained by the nebula rotation frequency (on the order of the Ekman length). The ratio of these quantities is the time scale of the turbulence, and gives the larger than expected value of Ω_e . In a normal Ekman layer, the *only* relevant time scale is that of the rotation. The significance of this distinction is primarily for the diffusion of particles. Specifically, our model for particle transport (Section 3, Appendix B) involves a diffusion coefficient which is a func-

tion of both the particle stopping time in the gas and the eddy frequency. We return to the potential implications of the overall process in Section 5.

By way of building credibility in these relationships, other quantities of interest can be estimated from them. For example, defining a typical (one-dimensional) turbulent velocity $v_T = f\Delta V = \sqrt{2k/3}$, we rewrite Eq. (26) as

$$\nu_T = \frac{c_\nu^4 c_\delta^4}{c_L^2} \frac{v_T^2}{f^2 \Omega} = \left(\frac{2c_\nu^4 c_\delta^4}{3c_L^2 f^2} \right) \frac{k}{\Omega}. \quad (35)$$

For comparison, we may rewrite Eq. (30) as

$$k = c_\mu^{-1/2} \nu_T \left| \frac{dV}{dz} \right| = c_\mu^{-1/2} \nu_T \text{Ro} \Omega$$

or

$$\nu_T = \frac{c_\mu^{1/2}}{\text{Ro}} \left(\frac{k}{\Omega} \right). \quad (36)$$

Comparing Eqs. (35) and (36) with (28) and solving for f , we find

$$f = \frac{c_\nu c_\delta}{c_L} \left(\frac{2}{3} \right)^{1/2} c_\mu^{-1/4} \approx 0.1, \quad (37)$$

adopting $c_\nu = 0.045$ (Coakely 1987), $c_\mu = 0.09$, $c_\delta = 2.5$, and $c_L = 1.5$. A rough fluid-dynamical rule of thumb states that in turbulence surrounding a jet, which is a 2-D analog to our situation near the midplane, $f \approx 0.05 - 0.1$ (Ruff and Faeth 1987). The agreement with the above scaling estimates is fairly good—the difference might even be entirely due to the difference between 1-D and 2-D geometry.

These scaling results provide physical justification for a simplifying assumption we noted in the previous section, namely that turbulence persists even very near the midplane where velocity shears formally vanish. A characteristic time scale t_T for transport of turbulence over vertical length scale z is on the order of $z^2/\nu_T = z^2/(L_E^2 \Omega) = (z/L_E)^2 \Omega^{-1}$. In contrast, turbulence is dissipated on a time scale $(2\pi/\Omega_e) = (c_\mu^{1/2} \text{Ro} \Omega)^{-1}$ from Eq. (33). Thus, turbulence can be transported into the midplane from shear production regions within $z \approx L_E (c_\mu u \text{Ro})^{-1/2} \approx 0.4 L_E$ on a time scale which is comparable to or shorter than its dissipation time, and one would expect turbulence to persist throughout the small part of the midplane region where the velocity gradient rigorously vanishes. This assumption of constant viscosity through the midplane has also been made by Weidenschilling and Cuzzi (1993), and we believe it is a reasonable approximation for the pres-

ent. Clearly, however, this aspect of the problem deserves more study. In the future we plan to employ more sophisticated turbulence models, but for the present adopt a canonical set of $c_\nu = 0.045$, $c_\delta = 2.5$, and $c_L = 1.5$.

2.3. Modeling Particle Dispersion; the Schmidt Number

The time-averaged particle momentum and mass Eqs. (9)–(11) involve correlation terms of the form $\overline{\rho_p' v_{pi}'}$, where ρ_p' is a fluctuation in particle density and v_{pi}' is the simultaneous fluctuation in the i th component of the particle velocity. Uncertainty as to how these terms should be modeled has presented significant difficulties to workers in other fields, leading most to abandon the Reynolds- or time-averaging technique altogether in favor of Favre- or mass-averaging (Champney and Cuzzi 1990; see also Appendix A) which removes them from the equations by definition.

However, we became dissatisfied with the Favre approach for the reasons detailed in Appendix A. Instead, we Reynolds-averaged all of the equations and retained the density correlation terms. We modeled these mass fluxes by the *gradient diffusion hypothesis* (GDH), widely used in engineering computational fluid dynamics. This assumes that the particle flux is proportional to the mean gradient of the particle density:

$$\overline{\rho_p' \mathbf{v}_p'} = D \nabla \overline{\rho_p}. \quad (38)$$

In turn, the diffusion coefficient D is proportional to the turbulent viscosity ν_T ,

$$D = \nu_T / \text{Sc}, \quad (39)$$

where the dimensionless coefficient Sc is called the Schmidt number (see Appendix B). For example, the particle continuity Eq. (15) may be written

$$\frac{\partial}{\partial t} \overline{\rho_p} + \frac{\partial}{\partial z} \left(\overline{\rho_p} \overline{w_p} - \frac{\nu_T}{\text{Sc}} \frac{\partial \overline{\rho_p}}{\partial z} \right) = 0. \quad (40)$$

2.3.1. The Schmidt number. The Schmidt number is usually considered to be a function of the Stokes number St , defined as

$$\text{St} \equiv t_s / Y, \quad (41)$$

where Y is called the *integral time scale* of the turbulence. Most researchers take $Y = 1/\Omega$ after Safronov (1969). However, as explained in Section 2.2.2, we believe that more generally $Y \approx \Omega_e^{-1} = c_\delta^2 c_\nu^2 \Omega^{-1}$. Safronov (1969) also assumed that a typical particle would develop a velocity fluctuation $u_p' \approx u_g'/(1 + \text{St})$; this implies

$$Sc = (1 + St)^2. \quad (42)$$

As shown in Appendix B, however, we have derived a formula (B15) for the Schmidt number that more fully captures the physics of particle interactions with a spectrum of turbulent eddies:

$$Sc = (1 + St)\sqrt{1 + 3\bar{w}_p^2/2k}. \quad (43)$$

Although it is not explicitly stated in their paper, Völk *et al.* (1980) obtained a similar functional form (but without the correction factor in \bar{w}_p). Equation (43) above also appears to be consistent with the theoretical results plotted in Figs. 6–8 of Canuto and Battaglia (1988). Figure 1 graphs Eqs. (42) and (43) for $\bar{w}_p = 0$, along with a numerical model and laboratory measurements of Sc versus St from Crowe *et al.* (1985). For the purpose of this paper, we are concerned primarily with large particles with $St > 1$. As the figure shows, the slope of Eq. (43) fits both the data and the numerical model in this region better than that of Eq. (42). Accordingly, we have adopted Eq. (43) as our basic prescription for the Schmidt number. For comparison, Fig. 2 shows Sc as a function of particle size for several locations in the nebula.

2.3.2. Drag coefficients. We have followed the formulation of drag coefficients by Weidenschilling (1977). The drag force on a particle of radius r_p depends on the size of the particle relative to the mean free path λ of a gas molecule ($\lambda \approx (r/1 \text{ AU})^{11/4} \text{ cm}$ in the model nebulae presented in Section 3),

$$F_D = \frac{C_D}{2} \pi r_p^2 \rho_g (\bar{\mathbf{v}}_p - \bar{\mathbf{v}}_g)^2, \quad r_p > \frac{9}{4} \lambda \quad (44)$$

$$F_D = \frac{4}{3} \pi r_p^2 \rho_g |\bar{\mathbf{v}}_p - \bar{\mathbf{v}}_g| c, \quad r_p < \frac{9}{4} \lambda, \quad (45)$$

where c is the thermal speed of the gas molecules. These are known as the Stokes and Epstein regimes, respectively. In the Stokes (large particle) regime, the drag coefficient C_D depends on the particle Reynolds number $Re_p = (2r_p|\bar{\mathbf{v}}_p - \bar{\mathbf{v}}_g|)/\nu_m$ of the flow past the particle as (for spheres):

$$C_D = 24Re_p^{-1}, \quad Re_p < 1; \quad (46)$$

$$C_D = 24Re_p^{-0.6}, \quad 1 < Re_p < 800; \quad (47)$$

$$C_D = 0.44, \quad Re_p > 800. \quad (48)$$

The stopping time t_s is then given by

$$t_s = \frac{m|\bar{\mathbf{v}}_p - \bar{\mathbf{v}}_g|}{F_D}. \quad (49)$$

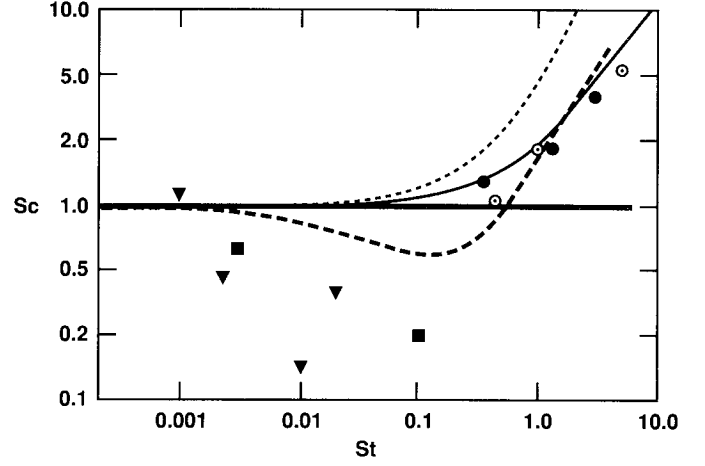


FIG. 1. Schmidt number Sc for particles of various sizes. Solid curve, our model (Eq. (43)) with $\bar{w}_p = 0$. Dotted curve, Safronov's model (Eq. (42)). Dashed curve, numerical model of Crowe *et al.* (1985). The various points are experimental data, taken from Crowe *et al.* (1985).

For $r_p \leq (9/4)\lambda_g$ (Epstein flow regime),

$$t_s = \frac{\rho_s r_p}{\rho_g c}. \quad (50)$$

For $r_p > (9/4)\lambda_g$ (Stokes flow regime),

$$t_s = \frac{8 \rho_s}{3 \rho_g C_D} \frac{r_p}{|\bar{\mathbf{v}}_p - \bar{\mathbf{v}}_g|}. \quad (51)$$

Note that the drag coefficient $A = (\rho_g t_s)^{-1}$ presented by Nakagawa *et al.* (1986, equation 24) in the Stokes regime

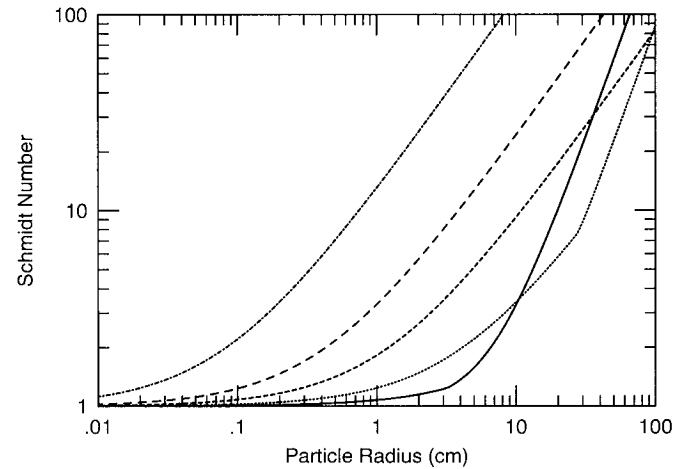


FIG. 2. Schmidt number Sc versus particle radius at several locations in a typical solar nebula (e.g., Hayashi 1981). Solid line, $r = 1 \text{ AU}$; dotted line, $r = 2.2 \text{ AU}$; short dash line, $r = 5 \text{ AU}$; long dash line, $r = 10 \text{ AU}$; dot-dash line, $r = 30 \text{ AU}$.

is a factor of 3/2 larger than that of Weidenschilling (1977), due to their use of a Maxwellian kinetic expression $\nu_m = (1/3)c\lambda$ for the kinematic viscosity instead of the more correct $(1/2)c\lambda$ (Kennard 1938, Rocard 1952). Furthermore, Nakagawa *et al.* (1986) use the $Re_p \leq 1$ expression, which is not valid for particles larger than about 10 cm at 1 AU or about 1 cm in circumplanetary nebulae; it is, however, valid to particle radii up to 1000 cm at 10 AU. Note also that t_s is independent of velocity for small particles, both in the Epstein flow regime (Eq. (50)) and in the Stokes regime for $Re_p \leq 1$ (Eq. (46)). For larger particles, F_D (and t_s) depend on the instantaneous velocity difference between the gas and particles, which rigorously includes turbulent velocity fluctuations. We have neglected this dependence in Appendix A, treating t_s as constant for the purposes of Reynolds averaging based on time scale arguments. However, our numerical technique allows the particle drag coefficient, stopping time, and Schmidt number (Section 2.3.1) to be varied in a self-consistent way as the particles settle or attain different velocities relative to the gas. In the models, we incorporate the effects of turbulent velocity fluctuations on the drag coefficients. We define a velocity scale for each location and particle size which is the quadratic sum of the mean drift velocity and gas turbulent velocity and use this scale in place of $|\bar{\mathbf{v}}_p - \bar{\mathbf{v}}_g|$ to determine the appropriate particle Reynolds number, the stopping time, and the Schmidt number.

2.4. The Numerical Approach

For the moment, we are studying a narrow annulus at an arbitrary radial location in the nebula, but nothing in the setup of the code prevents us from extending the code to two dimensions. The numerical model itself is used to solve for the first-order perturbed quantities described in Section 2.1. The radial and azimuthal components of the momentum equations detailed in Appendix A are solved in a nonconservative form. The nonconservative form is employed instead of the more commonly used conservative form to minimize roundoff errors. Roundoff errors may arise when the conservative variables (ρu , ρv , ρw , $\rho_p u_p$, $\rho_p v_p$, $\rho_p w_p$) are divided by the density (ρ , ρ_p) to obtain primitive variables (u , v , w , u_p , v_p , w_p). With the nonconservative form, this is avoided since we solve directly for the primitive variables. Zero gradient boundary conditions are assumed for the gas at the upper boundary of the grid and at the midplane. For the particles, zero gradient was assumed at the midplane but at the top of the grid the radial and azimuthal velocities are assumed to be the analytic values of Nakagawa *et al.* (1986) in the limit $\rho_p = 0$. Zero gradient boundary conditions were used at all radial boundaries. As noted earlier, we do not solve for the gas vertical velocity w . At an earlier stage in our modeling, we experienced difficulty with unstable

sound wave modes in the vertical direction. We avoided this problem by assuming that the vertical nebula pressure gradient maintains the gas in hydrostatic equilibrium with no significant vertical velocity. In the future we hope to relax this constraint.

Another stability problem was encountered in the vertical momentum equation of the particle phase, caused by the terms containing $\overline{\rho'_p w'_p}$ which originated from averaging the convection term (see Appendix A). However, it can be observed that, in the 1-D case, the particle continuity equation and the particle vertical momentum equation are coupled to the other two particle momentum equations only through the value of the turbulent viscosity. Because of this situation, we have adopted a hybrid solution scheme. The particle continuity and vertical momentum equations, which are strongly coupled, are solved simultaneously in a conservative form using first-order, upwind differencing for the convective terms and central differencing for the viscous terms. Then ρ_p and w_p are updated to the next time step, and the gas and particle radial and azimuthal momentum equations are solved in a nonconservative form using an explicit predictor-corrector scheme due to MacCormack (1969). This numerical approach was found to be more stable at the cost of some accuracy (however, as discussed below, the problem is not yet completely solved).

Due to residual numerical instabilities, we were forced to use one additional trick, and implement an adaptive coefficient approach to our most sensitive or stiff terms. By trial and error, we realized that most of our numerical difficulties arose from only two terms in the w_p equation (involving products of $\overline{w_p \rho'_p w'_p}$ and their derivatives). We decided on an approach where these two terms were multiplied by a stabilizing factor VCOEF, which rose from a value of 0.5 at an arbitrary initial state to a value of 1.0 when the particle vertical velocity began to vary by less than some specified fraction (10^{-4} to 10^{-7}) per time step.

We found that this approach allowed the numerical algorithm to avoid numerical instabilities and approach steady state for the cases presented in Section 4. However, we were not able to allow all cases to relax to the (rigorously correct) VCOEF = 1 at all vertical levels. The first case described in Section 4, (1 AU, 10 cm particle radius) did converge to a steady-state solution with VCOEF = 1 for all particle density values shown. That is, for $\rho_p > 10^{-4} \rho_g$, VCOEF = 1 and the equations being solved are exactly correct. For this case, we explored the implications of allowing the value of VCOEF to relax to 1.0 over different vertical ranges. We ran four cases with different convergence criteria, resulting in profiles of VCOEF which relaxed from 0.5 to 1.0 over a smaller range of altitudes. In the most extreme case, we forced VCOEF to remain at 0.5 throughout the entire vertical range. The vertical profiles for all quantities were indistin-

guishable. This is important because the cases involving larger particles exhibit more stubborn numerical instabilities; in most of these cases we were forced to keep our criterion for relaxing to $VCOEF = 1$ so restrictive (in terms of fractional change in vertical velocity) that the final value was never attained over a significant fraction of the vertical range. Effectively then, in these cases we solve a “more amenable” equation in regimes subject to numerical instability, with the coefficient of the troublesome term being half of the exact value. In all cases, the exact equation is operative for a range of grid points at the midplane and at the top of the grid. Similar substitution of a more “useable” equation for a more rigorously correct one was used by Shu *et al.* (1985, Eq. 82) in their analysis of nonlinear spiral density waves in planetary rings. Although we cannot, because of this lack of rigor, claim the solutions to be a precise match to reality in regions where the *approximately* correct set of equations is being solved, we believe that these solutions retain their physical significance. We base our belief primarily on the fact that the coefficient change from 0.5 to 1.0 produced *no discernible difference* in the 1-AU, 10-cm-radius profiles or in other cases where we have compared partially relaxed profiles with those in which $VCOEF$ was forced to remain at 0.5 throughout. Clearly, more work is needed to obtain an improved solution technique. It may be that time-like iteration needs to be replaced by space-like iteration; we intend to explore this in the future.

Since we are only interested in steady-state solutions, the small loss of temporal accuracy was not a concern. However, particle mass loss was observed in the results, caused by excessive numerical diffusion arising from the lack of spatial accuracy. Interestingly, a similar problem was noted by Sussman and Wilson (1991) for chemical flows, who solved the corresponding (particle) equation in logarithmic form. Unfortunately, this approach is not applicable to the two-phase flows studied here, because the phases (gas and particles) move at different velocities, whereas in the nonequilibrium flows of Sussman and Wilson (1991), all molecules in the mixture move at the same velocity. To compensate for the loss of particle mass in our calculation, an integrodifferential correction is applied periodically. In steady state, $\partial \bar{\rho}_p / \partial t = 0$, so that from the particle continuity Eq. (40),

$$\bar{\rho}_p \bar{w}_p - \frac{\nu_T}{Sc} \frac{\partial \bar{\rho}_p}{\partial z} = C, \quad (52)$$

where C is a constant. Evaluating the left side of Eq. (52) at $z = 0$ gives $C = 0$, while integrating it leads to the equality

$$\frac{\bar{\rho}_p(z)}{\bar{\rho}_p(0)} = \exp \left(\int_0^z \frac{Sc}{\nu_T} \bar{w}_p dz \right). \quad (53)$$

In the numerical model, the profile of $\bar{\rho}_p$ is updated using Eq. (53) above expressed at the current time step, and the value of $\bar{\rho}_p(0)$ is determined from the total particle mass. This correction is employed roughly every thousand time steps, and effectively speeds convergence to steady state while conserving mass by definition. No significant effect is noticed on the behavior of any of the other variables due to these occasional updates.

Our code must deal with particle density varying over more than 10 orders of magnitude. Several terms contain nondimensional gradients of the form $(1/\bar{\rho}_p) \partial \bar{\rho}_p / \partial z$, which can cause numerical difficulties at very small densities, where we know physically there is little effect. In the results presented in Section 4, we do not allow the particle density to fall below a certain minimum $\rho_{p,min}$ which may be varied. The specific value of this parameter does affect the detailed shape of the particle fall velocity profile at high altitudes, but not in a qualitative sense. For example, the very abrupt transition between “falling” and “steady-state” values of \bar{w}_p seems to be related to the choice of $\rho_{p,min}$. Physically, we believe in the reality of this transition; in actuality it may be less abrupt than seen in the model results. Smaller values of $\rho_{p,min}$ allow a smooth particle density profile to continue to larger altitudes and help the stability of the code in some situations; larger values are stabilizing in other regions of parameter phase space. Profiles in this paper assume $\rho_{p,min}$ at least 20 orders of magnitude smaller than that of the gas.

Finally, we treated particles with very long stopping times $t_s > \pi \Omega^{-1}$, which are underdamped, by an approximation also used by Weidenschilling (1984, 1988). In the underdamped case, particles oscillate about the midplane and are essentially executing inclined orbits. Gas drag slowly damps their inclinations, and a layer of such particles might be thought of as “settling” at the rate at which inclinations damp. Expressions for the inclination damping rate (Adachi *et al.* 1976) lead to an effective terminal settling velocity of z/t_s , which we substitute in our equations for the mean particle vertical velocity in this limit. That is, upward diffusion need only balance this slower settling velocity in order for the layer to have a steady-state vertical thickness. The actual instantaneous vertical velocity $z\Omega$ for such particles is used to correct the Schmidt number for streamline-crossing effects but is negligible compared to the radial and tangential velocities in calculating the velocity-dependent drag coefficients.

3. NEBULA MODEL PHYSICAL PROPERTIES

For the purpose of this work, we have adopted a simple formulation for the physical characteristics of the protoplanetary nebula. We take the total mass density $\sigma(r)$ and temperature $T(r)$ of the disk to be of the form

$$\sigma(r) = \sigma_0 \left(\frac{r}{r_0} \right)^{-p} \quad (54)$$

$$T(r) = T_0 \left(\frac{r}{r_0} \right)^{-q}, \quad (55)$$

where r_0 is a reference radius with Keplerian orbital frequency Ω_0 and velocity v_K . We assume that the disk is vertically isothermal at temperature $T(r)$.

The gas vertical scale height H is

$$\begin{aligned} H &= c/\Omega = \left(\frac{2R_g}{\mu} \right)^{1/2} T^{1/2} \Omega^{-1} \\ &= \left(\frac{2R_g}{\mu} \right)^{1/2} T_0^{1/2} \Omega_0^{-1} \left(\frac{r}{r_0} \right)^{3/2 - q/2} \equiv H_0 \left(\frac{r}{r_0} \right)^{3/2 - q/2}. \end{aligned} \quad (56)$$

The average gas density ρ_g (over a scale height) and gas pressure P are then

$$\rho_g = \frac{\sigma}{2H} = \frac{\sigma_0}{2H_0} \left(\frac{r}{r_0} \right)^{-(2p - q + 3)/2} \equiv \rho_0 \left(\frac{r}{r_0} \right)^{-s}. \quad (57)$$

For the purposes of this paper, the midplane gas density is taken to be the same as this average value. Also,

$$P = \frac{\rho_g R_g T}{\mu} = \frac{\rho_0 R_g T_0}{\mu} \left(\frac{r}{r_0} \right)^{-(s+q)}. \quad (58)$$

Nakagawa *et al.* (1986), following Adachi *et al.* (1976) designate the small perturbation to the radial force due to pressure support as η , where

$$\eta = - \left(\frac{1}{2\rho_g r \Omega^2} \right) \frac{\partial P}{\partial r} = \frac{(p + q/2 + 3/2) R_g T_0}{2r_0^2 \Omega_0^2 \mu} \left(\frac{r}{r_0} \right)^{(1-q)}. \quad (59)$$

One can obtain the reference surface mass density in terms of the global disk parameters by normalization:

$$\sigma_0 = \left(\frac{2-p}{2\pi R_0^2} \right) \left(\frac{R_D}{R_0} \right)^{p-2} M_D. \quad (60)$$

Combinations of observational evidence and theoretical expectations (e.g., Beckwith *et al.* 1990, Beckwith and Sargent 1991, Cassen 1992) lead one to consider a range

$$\frac{1}{2} < q < \frac{3}{4}, \quad 0 < p < \frac{5}{3}, \quad \text{and } T_0 \approx 200(1 + \sigma_0 \kappa)^{1/4} \approx 280 \text{ K},$$

where κ is the nebular opacity in the thermal infrared (Pollack *et al.* 1985, Ruden and Pollack 1991, Mizuno *et*

al. 1988, Cuzzi and Weidenschilling 1992, Miyake and Nakagawa 1992, 1993). For a quiescent protoplanetary nebula with parameters in this range, the perturbation parameter η is approximately 10^{-3} . In Table I we show some specific examples of η over a range of nebula parameters. Typically, nebula gas orbits at a local velocity $v_0 = v_K(1 - \eta)$.

In this paper, we use a standard “minimum mass” circumstellar nebula with $M_D = 0.0425 M_\odot$, $p = 1.5$, and $q = 0.5$. This leads to a total surface mass density $\sigma_0 \approx 1700 \text{ g cm}^{-2}$ at the reference radius of 1 AU. In the baseline model, the gas density at 1 AU is $1.4 \times 10^{-9} \text{ g cm}^{-3}$ and the temperature is 280 K. The molecular mean free path is about 1 cm, so most of the particles at 1 AU are in the Stokes drag regime (Section 2.3.2). Because it is too warm for water ice to condense, the minimum mass fraction of 5.3×10^{-3} gives the particles a surface mass density of about 9 g cm^{-2} . At 10 AU, the gas volume mass density is $2 \times 10^{-12} \text{ g cm}^{-3}$, the surface mass density is about 55 g cm^{-2} , the temperature is 90 K, and the particles, with all volatiles condensed, have surface density of about 0.6 g cm^{-2} . The molecular mean free path is about 600 cm, so most of the particles at 10 AU are in the Epstein drag regime (Section 2.3.2). We will also show some typical results for a circumstellar nebula with midplane temperature at 1 AU in the range of 1000 K. The global level of turbulence in such a hot nebula is unknown, so our neglect of any turbulence besides that driven by the particle layer is open to question. However, we include this case as an indication of the temperature sensitivity of our results.

4. RESULTS

We will present representative results which describe the behavior of the particle and gas phases near the midplane for a variety of particle radii and at a variety of nebula locations. First we quickly review the significant physics. Unperturbed particles orbit at the Keplerian rate; unperturbed gas at a pressure-supported rate. Mutual gas drag conveys orbital angular momentum from the particles to the gas, decreasing the orbital velocities of the particles and increasing that of the gas. This results in inward radial drifts for the particles and outward radial flow for the associated gas.

Up to this point, the physics is adequately captured by the analytical solutions of Nakagawa *et al.* (1986). We made a comparison between an early version of our code and the analytical solutions of Nakagawa *et al.* (1986) for a realistic range of nebula parameters, and good agreement was achieved even though we had to remove several advective terms from our model, and set the nebula viscosity to zero, in order to compare our results with their simplified formulation. Figure 3 compares particle

TABLE I

Variation of the Perturbation Parameter η (Eqs. (8) and (59)) with Nebula Location $r = 1, 10$, and 100 AU, Surface Mass Density Radial Variation Index p , Temperature Radial Variation Index q , and Midplane Temperature T_0 .

$T_0 = 280$ K					$T_0 = 1000$ K				
$r = 1$ AU					$r = 1$ AU				
$q = 0$					$q = 0$				
$T = 280$					$T = 1000$				
		0.5	1			0.5	1		
		280	280			1000	1000		
p	0.00	8.9E-04	1.2E-03	1.5E-03	p	0.00	3.2E-03	4.2E-03	5.3E-03
	0.33	1.1E-03	1.4E-03	1.7E-03		0.33	3.9E-03	4.9E-03	6.0E-03
	0.67	1.3E-03	1.6E-03	1.9E-03		0.67	4.6E-03	5.6E-03	6.7E-03
	1.00	1.5E-03	1.8E-03	2.1E-03		1.00	5.3E-03	6.3E-03	7.4E-03
	1.33	1.7E-03	2.0E-03	2.3E-03		1.33	6.0E-03	7.0E-03	8.1E-03
	1.67	1.9E-03	2.2E-03	2.5E-03		1.67	6.7E-03	7.7E-03	8.8E-03
$r = 10$ AU					$r = 10$ AU				
$q = 0$					$q = 0$				
$T = 280$					$T = 1000$				
		89	1			316	1		
		89	28			316	100		
p	0.00	8.9E-03	3.7E-03	1.5E-03	p	0.00	3.2E-02	1.3E-02	5.3E-03
	0.33	1.1E-02	4.4E-03	1.7E-03		0.33	3.9E-02	1.6E-02	6.0E-03
	0.67	1.3E-02	5.0E-03	1.9E-03		0.67	4.6E-02	1.8E-02	6.7E-03
	1.00	1.5E-02	5.6E-03	2.1E-03		1.00	5.3E-02	2.0E-02	7.4E-03
	1.33	1.7E-02	6.2E-03	2.3E-03		1.33	6.0E-02	2.2E-02	8.1E-03
	1.67	1.9E-02	6.8E-03	2.5E-03		1.67	6.7E-02	2.4E-02	8.8E-03
$r = 100$ AU					$r = 100$ AU				
$q = 0$					$q = 0$				
$T = 280$					$T = 1000$				
		28	1			100	1		
		28	2.8			100	10		
p	0.00	8.9E-02	1.2E-02	1.5E-03	p	0.00	3.2E-01	4.2E-02	5.3E-03
	0.33	1.1E-01	1.4E-02	1.7E-03		0.33	3.9E-01	4.9E-02	6.0E-03
	0.67	1.3E-01	1.6E-02	1.9E-03		0.67	4.6E-01	5.6E-02	6.7E-03
	1.00	1.5E-01	1.8E-02	2.1E-03		1.00	5.3E-01	6.3E-02	7.4E-03
	1.33	1.7E-01	2.0E-02	2.3E-03		1.33	6.0E-01	7.0E-02	8.1E-03
	1.67	1.9E-01	2.2E-02	2.5E-03		1.67	6.7E-01	7.7E-02	8.8E-03

Note. The nebula model is described in Section 3.

and gas velocities obtained from our code with the analytical results of Nakagawa *et al.* The velocities shown are relative to circular, equatorial motion at the Keplerian rate (for the particles) and relative to the pressure-supported orbital rate (for the gas). Also shown is the particle density profile which produces these velocities. The gas entrained within the dense particle layer near the midplane is driven to more rapid orbital velocity by drag with the particles. As the headwind experienced by individual particles decreases, particles locally cease their inward radial drift. Since the orbital velocity difference has not reached zero, the gas within the layer drifts radially outward relative to the surrounding gas; its radial pressure gradient still exists but it is receiving angular momentum from the particles. However, without inclusion of viscous, advective, and diffusion terms, no vertical transport of mass or momentum can be modeled, so the mean velocity profiles as well as the particle density profile remain undefined by this model.

Additional physics is included in the model we present here. Alteration of the vertical profile of gas velocity by the particle layer produces vertical wind shear, which generates turbulence and turbulent viscosity. The local viscosity ν_T and turbulent kinetic energy k are self-consistent functions of the local mean velocity gradients, using simple physically based models which incorporate experimentally determined parameters (section 2.2.1). Ensuing viscous stresses modify the vertical velocity distribution, and therefore feed back into the viscosity profile. The particle density is self-consistently determined by a balance between downward settling under gravity and upward diffusion in the local turbulence. The particle diffusion coefficient is related to the turbulent viscosity by the Schmidt number, which is a function of the local drag coefficients and eddy turnover frequency (Section 2.3). A fully self-consistent steady state is achieved in which the particle density profile generates sufficient turbulent diffusion to balance continual settling.

is a function of altitude, w_F is most simply understood only when the particle stopping time is short compared with the time it takes a particle to fall by a distance which changes its vertical acceleration significantly. This is the case in Figs. 4–6, but not in other cases to be shown.

One final function is shown with heavy long dashed lines; the effective *diffusion velocity* w_{diff} , which is defined as

$$w_{\text{diff}}(z) = \frac{v_T}{Sc} \frac{1}{\bar{\rho}_p} \frac{\partial \bar{\rho}_p}{\partial z}. \quad (62)$$

The quantity w_{diff} may be calculated from a simplified version of the particle continuity equation. That is, when the layer is in a steady state, Eq. (52) may be solved for the appropriate residual settling velocity w_p that can persist in the presence of upward diffusion. Note in Fig.

4 that there is excellent agreement between w_p and w_{diff} in the region below 35 km altitude; this tells us that the particle layer is in steady state throughout this vertical region—neither settling nor puffing up.

Recall that this is our numerically most well-behaved case (section 2.4) and achieves full convergence to the exact equations of motion at all levels of interest.

In Fig. 6, we compare the viscosity and density profiles for this case with a similar case in which we relaxed our artificial transport of viscosity into the midplane region (Sections 2.2.1 and 2.2.2). We tested this case because the vertical extent of the constant viscosity zone seemed rather large compared to the transport length scale estimated as $\sim 0.4L_E$ in Section 2.2.2. A single time step from a converged solution for each case is shown in Fig. 6; it is seen that the particle density profile does flatten slightly when turbulence is allowed to die out where the local velocity gradient gets small. However, the change is not significant.

Figures 7–9 show a more complex case at 1 AU for considerably more massive particles (60 cm radius). From Fig. 7, it is seen that the particle layer is considerably thinner than for the 10-cm particles, having a full layer thickness (at half maximum density) of only about 3000 km (compared to the 30,000-km thickness in Figs. 4–6). This is due to the relative difficulty of diffusing these more massive particles. Roughly speaking, the Schmidt number Sc here is about 10 times larger than for the 10-cm-radius particles, due to a combination of stopping time and eddy frequency effects, so from Eq. (62) one might argue simplistically that the equilibrium density gradient could be roughly 10 times larger. In fact, the peak particle density is now more than 10 times that of the gas (a local enhance-

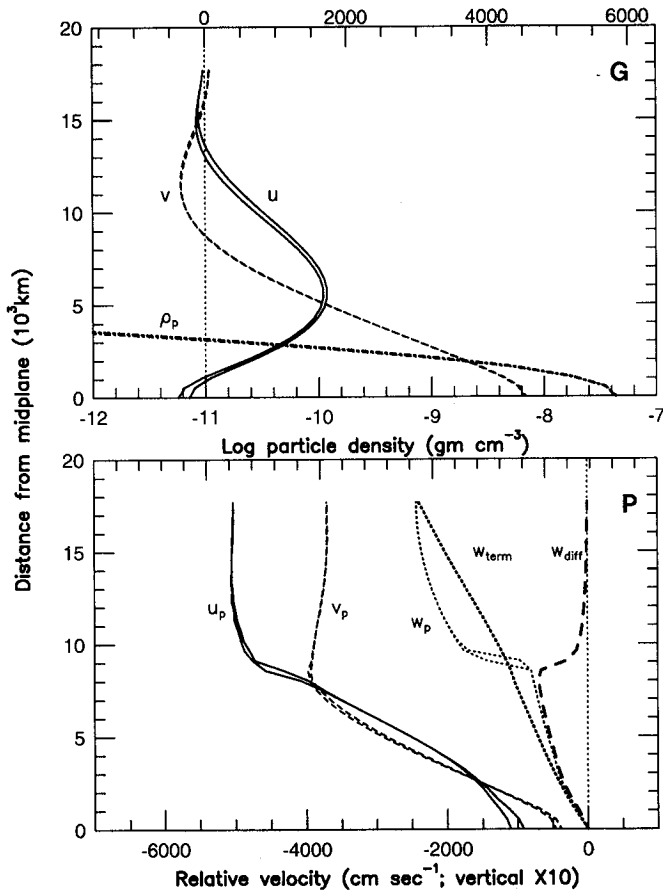


FIG. 7. Results for 60-cm-radius particles at 1 AU in the nebula, where the temperature is 280 K. Legend is as in Fig. 4, but here particle density profile is only shown in G (top). The run in this figure extended over about 0.5 years, after 5.2 years of evolution. As described in the text (Section 4.1), the top and bottom panels are horizontally shifted by the velocity difference $\Delta V = \eta v_k$. The gas mass density at this location is $1.4 \times 10^{-9} \text{ gm cm}^{-3}$. The vertical velocities w_p , w_{diff} , and w_F are expanded horizontally by a factor of 10.

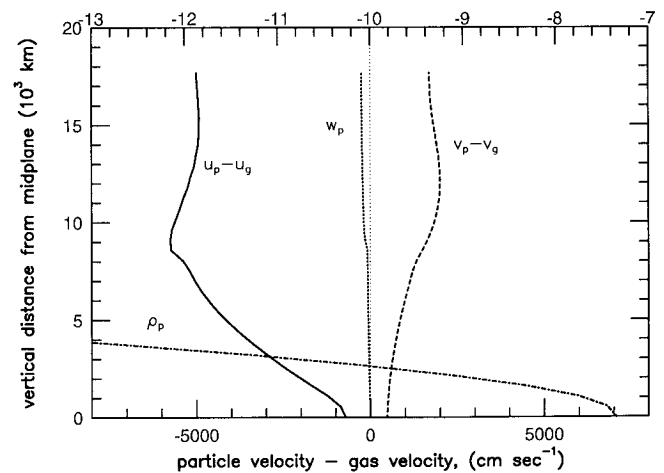


FIG. 8. Differential velocities for the model of Fig. 7. Solid curve, radial component; short dashed curve, azimuthal component; dotted curve, vertical component; dot-dashed curve, log particle mass density (upper horizontal axis).

ment of the solids/gas ratio by a factor of about 10^3 over cosmic abundance). Note, however, that the peak density is still about an order of magnitude too small for any sort of gravitational instability to occur (from Section 1, $\rho_{\text{crit}} \sim 3 \times 10^{-7} \text{ g cm}^{-3}$). Well above the midplane where the particle density is negligible, gas and particle velocities are essentially those of Weidenschilling (1977). Near the midplane, the massive particle layer drives the gas nearly to Keplerian velocity, and inward radial drifts for the particles decrease (as in Nakagawa *et al.* 1986). Velocity differences between particles and gas are shown in Figure 8.

Figure 7 demonstrates a strong outward flow of gas across the faces of the dense particle layer. This is due to exchange of angular momentum between the particles and the gas. These profiles are quite similar to those seen in the classical Ekman flow regime (e.g., Batchelor 1967, Holton 1972). Figure 9 repeats the particle density and gas velocity profiles from Fig. 7 and shows the vertical profile of gas *dynamic* viscosity $\mu_T = \rho_g \nu_T$ that results. Because the bulk of the mass in the particle layer is moving at a well-defined velocity, we may compare our numerical radial drift results with classical expressions for the shear stress on a disk in Ekman flow as discussed, for instance, by Goldreich and Ward (1973). The torque per unit area on the particle layer is $2rS$, where $S = \rho_g \nu_T dV/dz$ is the shear stress on each face of the particle layer. The torque is set equal to the divergence of the angular momentum flux, which may be approximated by $\sigma_p v_K \bar{u}_p$, and results in a drift velocity

$$\bar{u}_p = \frac{2S}{\Omega} \approx \frac{2\rho_g \Delta V^2}{\sigma_p \Omega \text{Re}^*}. \quad (63)$$

In the case of Figs. 7–9, with $\text{Re}^* = 55$, Eq. (63) above yields $\bar{u}_p \approx 700 \text{ cm sec}^{-1}$, close to the numerical results. The particle layer in this case is *optically* thin; its optical depth or area fraction covered is only about 0.02. The use of optical depth in this paper is unrelated to radiative properties, but is a measure of the fractional area covered by particles integrated over the layer.

The vertical velocity profiles of Figs. 7–9 show interesting differences from those in Figs. 4–6, in that w_p is never equal to the local terminal velocity w_{term} . This is due to a significant inertia effect, in which fairly large particles (such as those in Figs. 7–9 with stopping time $t_s \approx 2 \times 10^7 \text{ sec}$) carry the memory of the larger fall velocities they possessed at higher altitudes. That is, because the terminal velocity is a function of altitude, falling underdamped particles cannot be decelerated quickly enough to match the local w_{term} . We have examined the deviations of w_p from w_F seen at high altitudes and have found them to be reasonable. Note that the particle mean vertical velocity w_p (light dotted lines) switches from *faster* than

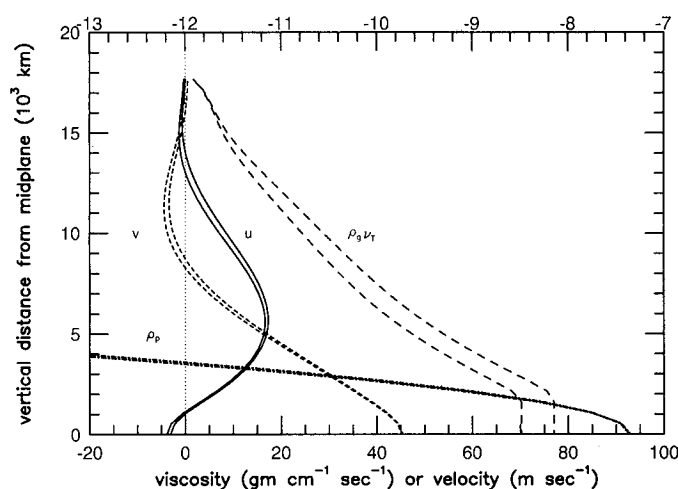


FIG. 9. Gas velocities and turbulent viscosity profile for the model of Fig. 7. Solid curve, radial component; short dashed curve, azimuthal component; long dashed curve, dynamic viscosity $\rho_g \nu_T$; dot-dashed curve, log particle mass density (upper horizontal axis). The different curves show extrema of typical (roughly epicyclic) variations in the profile through the run. Note: velocity scale is in m sec^{-1} instead of cm sec^{-1} .

w_F to *slower* than w_F at 9000 km altitude. This transition indicates where upward diffusion due to turbulence begins to play a role in slowing the particle settling rate. As noted in Section 2.4, however, the precise location and abrupt shape of the transition may be a numerical artifact.

Overall, however, and certainly in the high particle density regions, w_p and w_{diff} are in very good agreement, indicating a layer in steady state. We may quantify this somewhat using the residual vertical velocity difference $\bar{w}_p - w_{\text{diff}} \approx 1\text{--}2 \text{ cm sec}^{-1}$; at this rate the “lifetime” of the several-thousand-kilometer-thick layer to settling is on the order of tens of years, much longer than an orbit period or the nominal “terminal velocity” settling time scale. Even this is probably only a lower limit, due to the necessity to terminate runs before they reach genuine steady state.

Recall that all solutions other than those of Figs. 4–6 are obtained using equations which are slightly modified from the exact ones throughout a range of intermediate altitudes in order to avoid numerical instabilities. This issue was discussed in Section 2.4.

4.2. Model Results at 10 AU

Figures 10 and 11 show the behavior of a layer of 20-cm-radius particles at a distance of 10 AU from the star. Here, the gas density is $2 \times 10^{-12} \text{ g cm}^{-3}$, the temperature is about 90 K, and the particle surface mass density is only 0.6 g cm^{-2} . Qualitatively similar behavior is seen as for the 60-cm particle disk at 1 AU, but here the vertical length scale is larger. Note from Fig. 10 that the particle

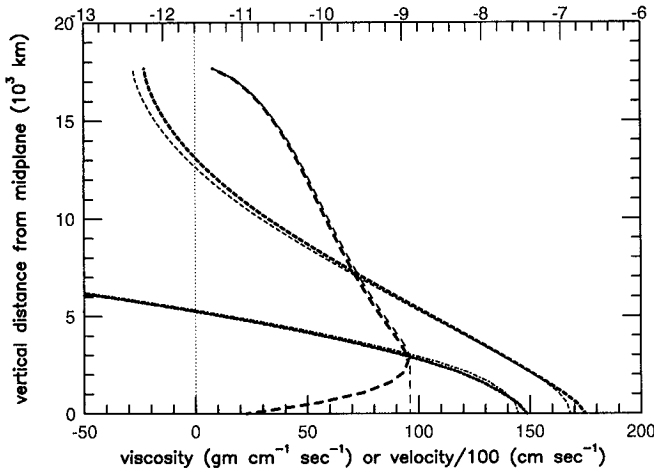


FIG. 16. Gas velocities and turbulent viscosity profiles for two models with the nebula and particle parameters of Fig. 14; legend is as in Fig. 6.

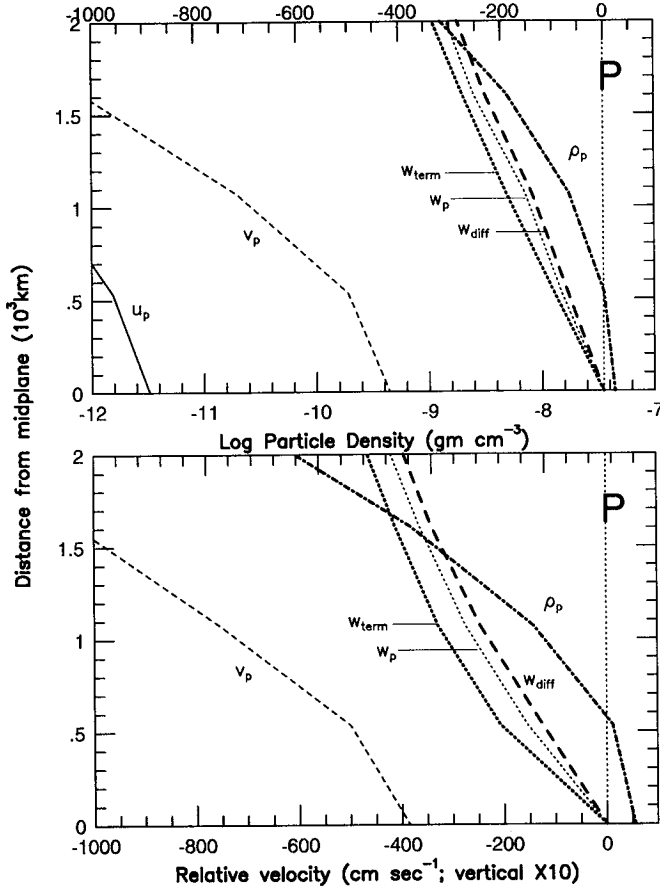


FIG. 17. Expanded plots of the region extremely close to the midplane, to illustrate the effect of particle layer self-gravity. This is the case of Fig. 7 (1 AU, 60-cm-radius particles). (Top) Without self-gravity; (bottom) with self-gravity. Self-gravity compresses the equilibrium particle layer only slightly, and the threshold for gravitational instability (3×10^{-7}) is not approached. Profile of u_p is off scale in bottom panel.

we compare profiles calculated with and without viscosity maintained constant across the midplane region; little significant difference is seen even in this case where the particles have stronger settling tendency than in Fig. 4–6.

4.4. Effects of Particle Layer Vertical Self-Gravity

Although we have found that particle densities do not get sufficiently large for gravitational instability to occur for any of the cases presented above, we did explore the effects of particle layer vertical self-gravity on the solutions. The expression for vertical gravity due to the particle layer at vertical location z of interest is taken as

$$g_z = 2\pi G \int_{-z}^z \rho_p(z') dz'. \quad (64)$$

Typical results are shown in Figs. 17 and 18. The effects are interesting; as one would expect, vertical self-gravity does play a role in compressing the layer somewhat; however, for the cases shown (1 AU, 60 cm particle radius

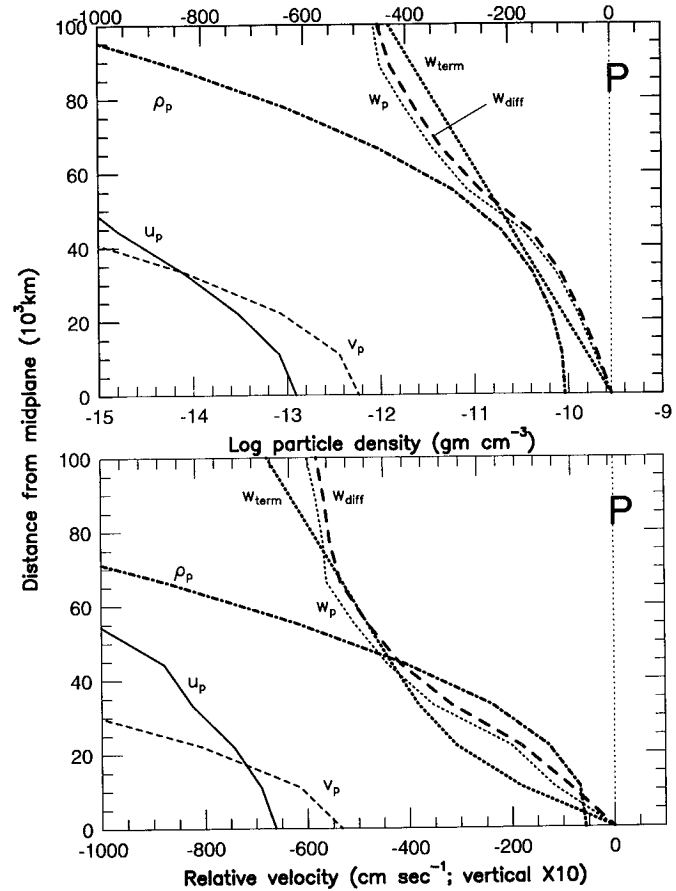


FIG. 18. As for Fig. 17, but for the case of Fig. 10 (10 AU, 20-cm-radius particles). Again, the threshold for gravitational instability at this location (3×10^{-10}) is not approached.

and 10 AU, 20 cm particle radius), the effect is too small to offset the role of turbulence in preventing the density from attaining any critical value. In one case shown earlier (Fig. 12; 10 AU, 60 cm particle radius) where the density was approaching its threshold value, we would expect the addition of self-gravity to nudge it higher, probably allowing it to exceed the threshold for axisymmetric instability. Generally speaking, then, inclusion of vertical self-gravity merely shifts the radial location or particle radius at which one might expect marginal (axisymmetric) gravitational instabilities to occur, but not by a very large amount. The layer must *already* be close to an unstable condition for this effect to come into play.

5. DISCUSSION

In this section we discuss some implications of our results for accretion of meteorite parent bodies and other primitive objects in the earliest stages of planetary formation. In the future we will present additional results for different assumed nebula properties, including global turbulence, particle size distributions, particle damping of turbulence, different midplane temperature, and so on. In most ways (except for the poorly understood global turbulence) we expect these future results to differ primarily in a quantitative sense.

5.1. Enhancement of Solid/Gas Ratio near the Nebula Midplane

First, of course, settled particle layers with lifetimes which appear to be long (relative at least to nominal particle settling times or orbit periods) provide an environment for planetesimal formation in which the solid/gas ratio is enhanced by one to three orders of magnitude compared to the well-mixed value of 10^{-2} . In the context of these models, an enhancement as large as $\sim 10^3$, in the range apparently required by some meteoritic oxidation states, does require a substantial fraction of the mass to have grown into particles of radius greater than 10 cm. For instance, the 10-cm-radius particles shown in Fig. 4 exceed the gas density only by a factor of a few, yielding an enhancement factor of a few hundred. The only way that subcentimeter chondrule-sized particles by themselves could ever attain significant enhancements by settling in this way to the nebula midplane would be if the nebula gas density were much less than the minimum mass value we have assumed.

One intriguing evolutionary scenario involves a potentially nonlinear settling stage. Smallish particles, which are easily supported in a layer of low vertical velocity gradient and therefore low viscosity and turbulent kinetic energy (perhaps even more extended than in Fig. 4), could reach a state in which further growth leads not only to increased settling *per se* but secondarily to sufficiently

increased velocity gradients and Rossby numbers that the eddy overturn frequency grows, increasing the particle Schmidt numbers (Section 2.3.1) and further decreasing the supportive capability of the turbulence. Such a situation has some aspects of an instability and is certainly worthy of further study. Coupled modeling of turbulent flow regimes, particle accumulation, and even radiative transfer is a desirable goal for the future.

5.2. Random Motions and Collision Velocities

We may estimate the random velocities of the particles in the midplane region using our calculated viscosity (for example, in Figs. 9, 10, and 12), its relationship to the turbulent kinetic energy k (Eq. (30)), and the definition of the Schmidt number Sc . From Eq. (B11) of Appendix B, the one-dimensional particle random velocity c_p is obtained from

$$c_p^2 \approx \frac{\overline{w'_p w'_p}}{w'_p w'_p} = \frac{\overline{w' w'}}{Sc} \approx \frac{2k}{3Sc} = \frac{2\nu_T \Omega Ro}{3c_\mu^{1/2} Sc} \approx \frac{2\nu_T}{3c_\mu^{1/2} t_s}. \quad (65)$$

For the case of Fig. 9 (1 AU, 60 cm particle radius), $\nu_T = \mu_T/\rho_g \approx 5 \times 10^{10} \text{ cm}^2 \text{ sec}^{-1}$, $Ro \approx 80$, and $Sc \approx 85$ (from the models, near the midplane), so $c_p \approx 140 \text{ cm sec}^{-1}$, consistent with a simple estimate $c_p \approx \Omega H_p$ from the full thickness H_p of the particle layer in Fig. 7. Particles with such large Schmidt numbers are poorly coupled to any particular eddy and thus uncorrelated with nearby particles of similar size. Therefore, this would be the collision velocity of 60-cm-radius particles in such an environment; their mutual collision times would be on the order of τ_p^{-1} times the orbit period, or roughly 50 years. Obtaining relative velocities in this way for smaller particles is not straightforward, since nearby objects are entrained in the same eddy (Völk *et al.* 1980).

5.3. Gravitational Instability Precluded

A summary of critical mass densities $\rho_{p,\text{crit}}$ required to achieve the *easiest* (axisymmetric) small-scale gravitational instability is given in Section 1. Good recent reviews have been presented by Weidenschilling *et al.* (1989), Wetherill (1990), and Safronov (1991). It is clear from the results of Figs. 4–16 that $\rho_{p,\text{crit}}$ is not achieved in any of our simulations at 1 AU and is approached at 10 AU only by particles of about 1 m in size. Another way to evaluate the stability at 1 AU, at least, is to note that the typical random velocities of 140 cm sec^{-1} of the previous subsection are nearly an order of magnitude larger than the value of $< 20 \text{ cm sec}^{-1}$ mentioned in Section 1. Our results thus confirm and extend the suggestions of Weidenschilling (1980), which were based on dimensional estimates of the properties of turbulence. Our results show particles of unit internal density growing to approximately 10^3 kg be

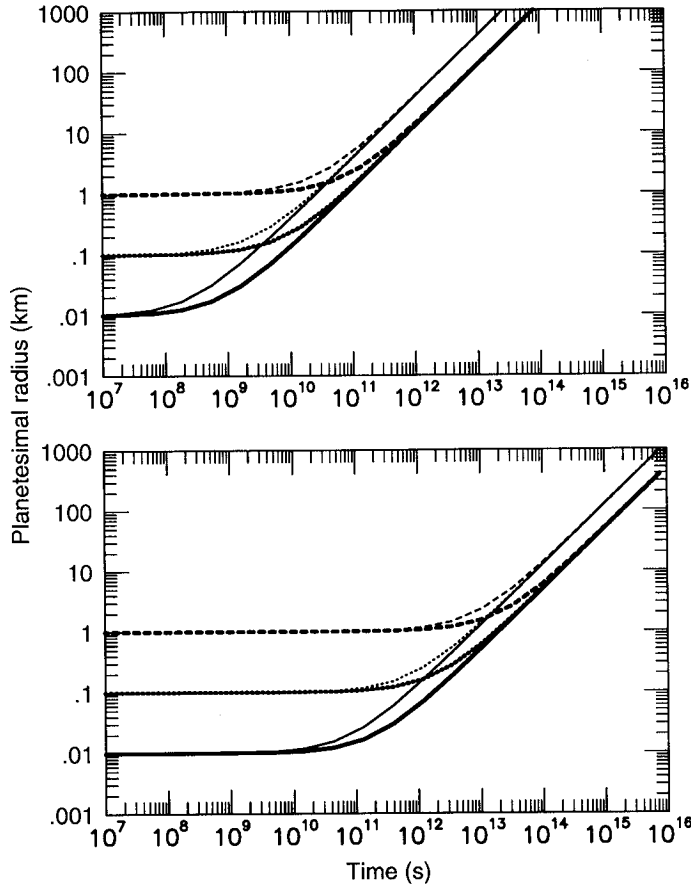


FIG. 19. Planetesimal radius as a function of time, for three different initial radii (solid, 10 m; dotted, 100 m; dashed, 1000 m); and two midplane environments. (Top) 1 AU ($\rho_s = 3$); heavy curves, 60-cm-radius particles as described in Fig. 7; light curves, 10-cm-radius particles as shown in Fig. 4. Mass growth is dramatic in a time comparable to or shorter than commonly accepted nebula lifetimes. For example, planetesimal radius of roughly 100 km is reached in less than 10^6 years, regardless of initial radius. (Bottom) 10 AU ($\rho_s = 1$); light curves, 20-cm-radius particles as described in Figs. 10 and 11; heavy curves, 60-cm-radius particles as shown in Figs. 14 and 15.

of Fig. 7, and about an order of magnitude smaller for the 10-cm-radius case of Fig. 4.

Solutions to the growth Eq. (70) for different values of r_{p0} , and the midplane environments of Figs. 4 and 7 at 1 AU, are shown in Fig. 19 (top). At 1 AU, anything larger than about 10 m radius grows by accretion to a radius of roughly 100 km in about 10^5 years, assuming that all conditions remain constant; as seen in Fig. 19 (bottom), growth takes longer at 10 AU. Solutions to the drift Eq. (72) are shown in Figs. 20 (top) and 20 (bottom); it is clear that mass growth limits the distance which a growing planetesimal will drift. In either of the 1-AU environments, planetesimals grow so fast that they do not drift more than about 10^{-2} AU from their initial location! The situation is similar at 10 AU. These radial drift results are

smaller than noted by Weidenschilling (1988), because of the smaller mass growth associated with his smaller assumed midplane particle mass densities ($\bar{\rho}_p = \rho_g$). This growth effect is also distinct from that of Nakagawa *et al.* (1983) in which only 10-km planetesimals were considered and in which the only role of gas drag was to replenish planetesimal feeding zones.

We can compare planetesimal growth rates due to differential drift with those estimated using the standard binary accretion formulae (Safronov 1972, Lissauer 1987, Wetherill 1990). The binary collision growth time $t_{m,b}$ may be approximated by

$$t_{m,b} = m_p \left(\frac{dm_p}{dt} \right)^{-1} \approx \frac{4\rho_s r_p}{f_G \sigma_p \Omega}, \quad (73)$$

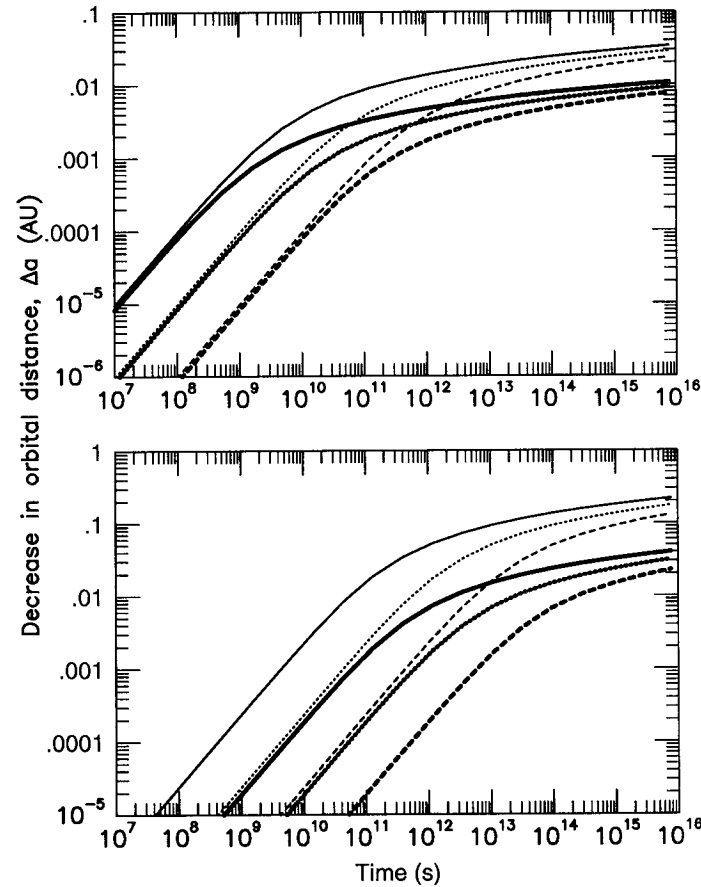


FIG. 20. Planetesimal radial excursions Δr as a function of time; (top). Results at 1 AU ($\rho_s = 3$) for three different initial radii (solid, 10 m; dotted, 100 m; dashed, 1000 m) and two different midplane environments (heavy curves, 60-cm-radius particles as described in Fig. 7; light curves, 10-cm-radius particles as shown in Fig. 4). The linear drift regime at times less than 10^2 years or so corresponds to the simple expression in Eq. (68); however, in all cases, the drift rate decreases because of mass growth, and the ultimate radial decay of such a planetesimal is no more than about 10^{-2} AU. (Bottom) Similar results at 10 AU, as in Fig. 19 ($\rho_s = 1$).

where $f_G \approx V_{\text{esc}}^2 / \Delta V_p^2$ is the gravitational focusing factor, with $V_{\text{esc}} = (2Gm_p/r_p)^{1/2}$ being the gravitational escape velocity of the growing planetesimal. It seems to us that the typical relative velocity $\Delta V_p \approx 10^3 \text{ cm sec}^{-1} \gg c_p \approx 10^2 \text{ cm sec}^{-1}$ is sufficiently small for simple sticking to be reasonable. That is, the lower relative velocities in the midplane, due to collective effects ($\Delta V_p \ll \eta v_K$), mitigate somewhat the uncertainties about the relative roles of mass accretion and removal during this stage (e.g., Wetherill 1990). These velocities are also too large for gravitational focusing to be relevant until the planetesimal grows to 10 km radius or so. The ratio of the drift-augmented accretion and simple binary accretion time scales is then

$$\frac{t_{m,d}}{t_{m,b}} = \frac{f_G \sigma_p \Omega}{3 \rho_p \Delta V_p}. \quad (74)$$

For the case of Fig. 7, the ratio is roughly $f_G/300$, and for the case of Fig. 4, it is about three times smaller. That is, in the 60-cm particle layer, the drift-augmented accretion time scale is faster than the local “binary” accretion time scale until the gravitational focusing factor of the growing planetesimal exceeds 300. This requires the planetesimal to grow (presumably by drift-augmented accretion) to a radius $r_p > 140 \text{ km}$ for $\rho_s = 3$ and $\Delta V_p \approx 1000 \text{ cm sec}^{-1}$. The very limited radial decay of these accreting objects allows us to consider them as essentially fixed, while the “particle disk” in which they are embedded drifts rapidly inward past them. That is, in the 10^5 – 10^6 years or so that it takes for the above simple planetesimal growth scenario to unfold, the sub-meter-size disk material, drifting inward at a rate of approximately 50 to 1000 cm sec^{-1} (10^{-4} to $2 \times 10^{-3} \text{ AU year}^{-1}$), could migrate tens or even hundreds of astronomical units.

To study the fate of the drifting material, imagine a critical stage to be that at which the mass in planetesimals is comparable to the mass in the meter (or smaller) sized particles. Prior to this, we might think of the midplane as being “particle disk dominated,” with behavior simply modeled as in Figs. 4 to 16. Toward the end of planetesimal accretion, one might think of the midplane as “planetesimal dominated” and model it using N-body dynamics. During the intermediate stage, significant planetesimal growth occurs within a drifting particle layer. We can estimate the probability (during the intermediate stage) that inwardly evolving disk material will encounter *some* planetesimal in the region $r < 2 \text{ AU}$, rather than being lost into the Sun. Half of the optical depth of the particle disk of Fig. 7, for example, is about 10^{-2} . The optical depth of a comparable mass of planetesimals of radius r_p is $\tau_p \approx \tau_p r_p / r_p \approx 10^{-5}$ ($1 \text{ km}/r_p$) if we assume comparable internal densities.

The individual particles within the layer, moving vertically at their random relative velocity c_p , traverse the

midplane and its optically thin layer of planetesimals twice every orbit period. During the τ_p^{-1} crossings that must occur before a planetesimal is physically encountered and the particle accreted, the disk particles incur a radial decay by

$$\Delta r_{\text{acc}} \approx \tau_p^{-1} \bar{u}_p \frac{2\pi}{\Omega}. \quad (75)$$

Thus, in drifting some arbitrary distance Δr , a fraction $F_{\text{acc}} \approx \Delta r / \Delta r_{\text{acc}}$ of the disk particulates is absorbed. The cases of Figs. 7 and 10 span a range in $\bar{u}_p \approx 50$ to 1000 cm sec^{-1} . Then in traversing a radial range of 2 AU , the fraction accreted is $F_{\text{acc}} \approx (0.01\text{--}1)$ ($1 \text{ km}/r_p$), for roughly meter-radius and few-centimeter-radius particles, respectively. The smaller particles drift more slowly and thus must traverse the planetesimal layer more often in drifting a certain radial distance, increasing their probability of being accreted.

Qualitatively taking this line of speculation even one step further, if this sort of growth scenario is correct, one might expect growing planetesimals to acquire an inhomogeneous radial structure and/or mineralogy, accumulating condensed material which originated from successively cooler regions of the nebula. These estimates assume perfect sticking, and the details will depend on initial conditions to some extent. Eventually, such simplistic “evolutions” will become quantitatively invalid due to changing midplane conditions by the time the mass in “planetesimals” becomes much larger than that in the particle disk. Thus, more detailed modeling would be useful.

5.5. Outward Motion of Gas, and Entrained Grains and Chips

The gas velocity profiles in Figs. 7, 10, and 12 show that streams of outward moving gas flow across the upper and lower surfaces of the settled particle layer at a peak relative velocity (at 1 AU) of about $\eta v_K/2$ (20 m sec^{-1} at 280 K , or 50 m sec^{-1} at 1000 K). This suggests another possible mechanism for radial mixing of both solid and gaseous material from different thermal and compositional regimes.

Small solid particles with $\text{St} \ll 1$ will be borne outward in the systematic outward flow, while traversing the particle layer within individual turbulent eddies. In the case of Figs. (4)–(16), the “large” particle layer has a small areal coverage fraction of particles $\tau_p \approx \sigma_p / \rho_s r_p$, where τ_p is the normal optical depth. Each time small grains and chips traverse the midplane in their gas eddies, they have a probability τ_p of encountering a large particle and being accreted. Below we estimate the range of outward motion Δr (relative to the inwardly drifting particles) that a typical small grain might experience.

The interval between crossings of the particle layer is $\sim L_E^2/\nu_T \approx \Omega^{-1}$. During the τ_p^{-1} crossings that must occur before the chip is accreted onto a larger particle, its relative radial excursion is (at 1 AU)

$$\Delta r \approx \tau_p^{-1} \frac{L_E^2}{\nu_T} (\bar{u}_g - \bar{u}_p) \approx \frac{(\bar{u}_g - \bar{u}_p)}{\Omega \tau_p}, \quad (76)$$

where $\bar{u}_g - \bar{u}_p$ is the differential mean velocity in the regions above the concentrated particle layer. We assume meter-sized particles in calculating $\tau_p \approx 10^{-3}$ and evaluate Eq. (76) above for the 280 K and 1000 K nebulae of Figs. 7 and 14, respectively, to obtain $\Delta r \approx 2\text{--}5$ AU! This process might be of relevance in understanding the mixture of high- and low-temperature minerals found in certain meteorite classes. Essentially, small, high-temperature fragments can be carried outwards to mix with large, lower-temperature ensembles which are drifting inwards. The cases in Figs. 7, 10, and 12, in which the particle layer is optically thin and well settled, provide a larger estimate for the range over which such chips might be transported than a case such as Fig. 4 in which the optical depth is larger and the outward flow is less dramatic. Thus the radial mixing process might vary in strength with the stage of planetesimal growth.

From the standpoint of volatiles, one might imagine that a systematic flow of warm gas outward across a condensation front could significantly enhance the local concentration of solid material. A process similar to this was advocated by Stevenson and Lunine (1988); they suggested normal diffusion of warm, water-vapor-bearing gas outward across a condensation boundary. Their suggestion involved radial *diffusion* averaged throughout the entire vertical scale height of the gaseous nebula, whereas in contrast, our results imply radial *advection* within a thin boundary layer region. An estimate of the amount of water vapor that could be carried across the water condensation front by advection is

$$\frac{d}{dt} m_{\text{H}_2\text{O}} \approx 2\pi r L_E \mu_g \rho_g f_{\text{H}_2\text{O}}. \quad (77)$$

At 5 AU, if $\rho_g \approx 10^{-11} \text{ g cm}^{-3}$, $L_E \approx 10^{10} \text{ cm}$, $f_{\text{H}_2\text{O}} = 5 \times 10^{-3}$, and $\bar{u}_g \approx 3 \times 10^3 \text{ cm sec}^{-1}$, $(d/dt)m_{\text{H}_2\text{O}} \approx 10^{-5} M_\oplus \text{ year}^{-1}$. This amount of solid material could contribute meaningfully to formation of Jupiter's core if it were all to remain on the cold side of the condensation front.

However, a complication here, as with the mechanism of Stevenson and Lunine (1988), is the offsetting inward motion of the condensate. A full model of gas and particle motions in the vicinity of a condensation front, where a significant volatile such as H_2O changes state between gas and solid, is probably needed. Outwardly drifting, water-laden gas will cool and condense solid material,

either into grains or upon preexisting, inwardly drifting objects. Also, objects formed cold at larger radii drift inward across the boundary, becoming warmer and possibly undergoing compositional alteration before releasing their volatiles to drift back outward. Interesting compositional and fluid dynamical effects could occur simultaneously (due to radial gradients of particulate mass density). These are appropriate subjects for future study.

5.6. Uncertainties and Future Work

An improved parametrization of the turbulent kinetic energy, with important implications for diffusion terms in the momentum equations and for eddy overturn frequencies in the Schmidt number model, is clearly a first step. In making this improvement, we expect to include all terms dealing with turbulence production, transport, and dissipation using a full k -equation model (e.g., Rodi 1980, Champney and Cuzzi 1989) and incorporate within it a model of particle damping of turbulence as well. This equation may be derived and modeled using a straightforward extension of the techniques we have developed for modeling time-averaged correlation terms (Appendices A and B). The fundamental constant c_ν (Section 2.2.1) is probably worthy of further investigation, perhaps in the laboratory. Also, we need to model the behavior of a distribution of particle sizes (or at least a few diverse particle sizes) simultaneously. Realistic coagulation models (Weidenschilling 1988, Weidenschilling and Cuzzi 1993) indicate that the first meter-sized particles arrive at the midplane while the bulk of the solids still remain dispersed in particles too small to settle significantly. The implications of global turbulence in addition to our local boundary layer turbulence could be considered in more detail; any additional contribution from global turbulence would lead to more vertically extended particle layers. However, quantification of global turbulence is extremely uncertain at present. Other nebula parameters need to be explored, including the qualitatively similar but quantitatively different circumplanetary nebulae within which the satellites of the outer Solar System probably form.

6. CONCLUSIONS

We have developed a methodology for self-consistently modeling the dynamical and structural properties of a fully viscous, coupled, two-phase circumstellar or circumplanetary nebula, in which the gas is pressure supported and the particles are coupled to the gas only by drag forces. We use the Reynolds-averaged Navier–Stokes equations, including compressibility for the particle phase. We have developed a new model of particle diffusivity in turbulence (our Schmidt number model). Our numerical solutions have many of the characteristics of Ekman flow, at least in the limit where the particles are

highly settled (layer thickness $\sim 10^{-4}$ of the gas scale height). Our conclusions are that particle layers, although highly settled relative to the gas (by an enhancement factor of $10\text{--}10^3$) *do not* attain the large mass volume densities (small random velocities) which are needed for the layers to be gravitationally unstable in the Goldreich-Ward sense (direct collapse to solid planetesimals on dynamic time scales), at least until they have grown by other means to masses comparable to most meteorite samples. On the other hand, rapid accretion of 100-km-radius planetesimals occurs within such an environment with very little associated radial drift, as a direct result of differential gas drag. Finally, outwardly directed transport of solid chips and volatiles coupled with inward-directed transport of larger particles could lead to significant radial compositional mixing and localized mass enhancements.

APPENDIX A: REYNOLDS AVERAGING

It is most convenient to cast the equations describing the Solar nebula in a cylindrical coordinate system (r, θ, z) . The corresponding velocity components are (u_g, v_g, w_g) for the gas phase and (u_p, v_p, w_p) for the particles. In these coordinates, conservation of mass is expressed by the continuity equation

$$\frac{\partial}{\partial t} \rho + \frac{1}{r} \frac{\partial}{\partial r} (r\rho u) + \frac{1}{r} \frac{\partial}{\partial \theta} (\rho v) + \frac{\partial}{\partial z} (\rho w) = 0, \quad (\text{A1})$$

where t is time and ρ is either ρ_g or ρ_p , the mass density of the gas or of the particles, respectively.

The momentum equations may be stated in either conservative or nonconservative form. As explained below, the conservative form is the preferred point of departure. In our coordinates, these become

$$\begin{aligned} \frac{\partial}{\partial t} (\rho u) + \frac{1}{r} \frac{\partial}{\partial r} (r\rho u^2) + \frac{1}{r} \frac{\partial}{\partial \theta} (\rho uv) + \frac{\partial}{\partial z} (\rho uw) = -\frac{\partial}{\partial r} P - \rho G M r / R^3 \\ + \rho v^2 / r \pm \rho_p (u_p - u_g) / t_s \end{aligned} \quad (\text{A2})$$

$$\begin{aligned} \frac{\partial}{\partial t} (\rho v) + \frac{1}{r} \frac{\partial}{\partial r} (r\rho uv) + \frac{1}{r} \frac{\partial}{\partial \theta} (\rho v^2) + \frac{\partial}{\partial z} (\rho vw) = -\frac{1}{r} \frac{\partial}{\partial \theta} P - \rho uv / r \\ \pm \rho_p (v_p - v_g) / t_s \end{aligned} \quad (\text{A3})$$

$$\begin{aligned} \frac{\partial}{\partial t} (\rho w) + \frac{1}{r} \frac{\partial}{\partial r} (r\rho uw) + \frac{1}{r} \frac{\partial}{\partial \theta} (\rho vw) + \frac{\partial}{\partial z} (\rho w^2) = -\frac{\partial}{\partial z} P - \rho G M z / R^3 \\ \pm \rho_p (w_p - w_g) / t_s, \end{aligned} \quad (\text{A4})$$

where G is the Newtonian constant of gravitation, M is the mass of the Sun, and $R \equiv \sqrt{r^2 + z^2} \approx r$ is the distance from the Sun. For the gas phase, P is simply the thermodynamic pressure and the symbol \pm is a plus sign, but for the particle phase $P = 0$ while \pm is a minus sign. In either case, t_s is the stopping time of the particles in the gas, inversely proportional to their drag coefficient. Equations (A2)–(A4) above are just the Navier-Stokes equations in conservative form, with the molecular viscosity terms replaced by the frictional coupling between the phases.

In order to separate the long-term time evolution of the nebula from short-term turbulent fluctuations, we use the technique of Reynolds averaging. First, the dependent variables in (A1)–(A4) are expanded into means and variations,

$$\rho = \bar{\rho} + \rho', \quad u = \bar{u} + u', \quad v = \bar{v} + v', \quad w = \bar{w} + w', \quad P = \bar{P} + P', \quad (\text{A5})$$

where the overbar denotes a short-term time average and the prime signifies a short-term fluctuation. For example, expanding Eq. (A1) in this manner gives

$$\begin{aligned} \frac{\partial}{\partial t} (\bar{\rho} + \rho') + \frac{1}{r} \frac{\partial}{\partial r} (r\bar{\rho}\bar{u} + r\rho'\bar{u} + r\bar{\rho}u' + r\rho'u') \\ + \frac{1}{r} \frac{\partial}{\partial \theta} (\bar{\rho}\bar{v} + \rho'\bar{v} + \bar{\rho}v' + \rho'v') \\ + \frac{\partial}{\partial z} (\bar{\rho}\bar{w} + \rho'\bar{w} + \bar{\rho}w' + \rho'w') = 0. \end{aligned} \quad (\text{A6})$$

Next the equations themselves are averaged over short time scales. This averaging removes short-period terms involving only one primed quantity, since $\bar{\rho'} = \bar{u'} = \bar{v'} = \bar{w'} = \bar{P'} = 0$. However, correlations between two or more fluctuations do not vanish in general. Furthermore, azimuthal derivatives $\partial/\partial\theta$ of averaged quantities can be neglected by the assumption of rotational symmetry. Then (A6) above reduces to

$$\frac{\partial}{\partial t} \bar{\rho} + \frac{1}{r} \frac{\partial}{\partial r} (r\bar{\rho}\bar{u} + \overline{r\rho'u'}) + \frac{\partial}{\partial z} (\bar{\rho}\bar{w} + \overline{\rho'w'}) = 0. \quad (\text{A7})$$

The momentum Eqs. (A2)–(A4) are treated similarly.

Note the presence in (A7) of the density correlations $\overline{\rho'u'}$ and $\overline{\rho'w'}$. These also appear in the Reynolds-averaged momentum equations, along with $\overline{\rho'v'}$ and various other correlations. Thus the evolution of the mean density and velocity fields depends on their fluctuations. This is an example of the closure problem in turbulence studies. In general, these correlations must be modeled in terms of the mean flow. This situation is somewhat simpler for the gas than for the particle phase, because velocities in the gas are much less than the speed of sound. Then the gas behaves as an incompressible fluid, so $\rho_g = \bar{\rho}_g$ and its density variation ρ'_g may be neglected. This approximation does not apply to the particle phase, however, which behaves as a very compressible fluid.

Compressible fluids are often treated by a somewhat different technique, called mass-weighted or Favre averaging (Cebeci and Smith 1974). In Favre averaging, the density and pressure are expanded into mean and fluctuating parts $\rho = \bar{\rho} + \rho'$, $P = \bar{P} + P'$ just as in Reynolds averaging, but the velocity components are expanded as

$$u = \bar{u} + u'', \quad v = \bar{v} + v'', \quad w = \bar{w} + w'', \quad (\text{A8})$$

where

$$\begin{aligned} \bar{u} &\equiv \overline{\rho u} / \bar{\rho} = \bar{u} + \overline{\rho'u'} / \bar{\rho}, \quad u'' = u' - \overline{\rho'u'} / \bar{\rho}, \\ \bar{v} &\equiv \overline{\rho v} / \bar{\rho} = \bar{v} + \overline{\rho'v'} / \bar{\rho}, \quad v'' = v' - \overline{\rho'v'} / \bar{\rho}, \\ \bar{w} &\equiv \overline{\rho w} / \bar{\rho} = \bar{w} + \overline{\rho'w'} / \bar{\rho}, \quad w'' = w' - \overline{\rho'w'} / \bar{\rho}. \end{aligned} \quad (\text{A9})$$

Then the equations are time-averaged as before. For example, Favre-averaging Eq. (A1) gives

$$\frac{\partial}{\partial t} \bar{\rho} + \frac{1}{r} \frac{\partial}{\partial r} (r\bar{\rho}\bar{u}) + \frac{\partial}{\partial z} (\bar{\rho}\bar{w}) = 0. \quad (\text{A10})$$

Equation (A10) above is ostensibly simpler than (A7), because (A10) contains no explicit correlation terms which require modeling. The Favre-averaged momentum equations still contain six velocity correla-

tions of the form $\overline{u''u''}$, $\overline{u''v''}$, etc., but are also much simpler than the corresponding Reynolds-averaged equations. The drawback to Favre averaging is the interpretation of the mean velocity. Turbulent mixing should cause diffusion of particles, even when their average velocity vanishes. Equation (A7) can model this behavior through the correlation terms, but (A10) cannot. As a consequence, our earlier work (Champney and Cuzzi 1990) used a hybrid approach due to Coakley and Champney (1985) where the continuity Eq. (A1) was Reynolds-averaged, but the momentum Eqs. (A2)–(A4) were Favre-averaged. This led to serious doubts of internal consistency and some spurious results, e.g., Fig. A1. Consequently, we have recast the entire system in a consistent Reynolds-averaged form.

Reynolds averaging the nonconservative form of the momentum equations generates correlations of the form $\overline{u'(\partial/\partial r)u'}$, $\overline{w'(\partial/\partial z)u'}$, etc. It was in order to avoid such terms that we Reynolds averaged the momentum equations in the conservative form (A2)–(A4). As explained in the text, however, we found by experience that a nonconservative form of the averaged horizontal momentum equations led to better accuracy. These were obtained by subtracting \bar{u} times Eq. (7) from the Reynolds-averaged version of Eq. (2) and \bar{v} times Eq. (7) from the Reynolds-averaged version of Eq. (3). The resulting equations take the form

$$\begin{aligned} \bar{\rho} \frac{\partial}{\partial t} \bar{u} + \frac{\partial}{\partial t} \overline{\rho' u'} + \bar{\rho} \bar{u} \frac{\partial}{\partial r} \bar{u} + \bar{\rho} \bar{w} \frac{\partial}{\partial z} \bar{u} = & -\frac{\partial}{\partial r} \bar{P} - \bar{\rho} G M r / R^3 + \bar{\rho} \bar{v}^2 / r \\ & + \frac{1}{r} \frac{\partial}{\partial r} (r \sigma_{rr}) + \frac{\partial}{\partial z} \sigma_{rz} - \sigma_{\theta\theta} / r + 2 \overline{\rho' v' \bar{v}} / r - 2 \overline{\rho' u' \bar{u}} \frac{\partial}{\partial r} \bar{u} \\ & - \bar{u} \frac{1}{r} \frac{\partial}{\partial r} (r \overline{\rho' u'}) - \overline{\rho' w'} \frac{\partial}{\partial z} \bar{u} - \frac{\partial}{\partial z} (\overline{w \rho' u'}) \\ & \pm [\bar{\rho}_p (\bar{u}_p - \bar{u}_g) + \overline{\rho'_p u'_p} - \overline{\rho'_p u'_g}] / t_s, \end{aligned} \quad (\text{A11})$$

$$\begin{aligned} \bar{\rho} \frac{\partial}{\partial t} \bar{v} + \frac{\partial}{\partial t} \overline{\rho' v'} + \bar{\rho} \bar{u} \frac{\partial}{\partial r} \bar{v} + \bar{\rho} \bar{w} \frac{\partial}{\partial z} \bar{v} = & -(\bar{\rho} \bar{u} + \overline{\rho' u'}) \bar{v} / r + \frac{1}{r} \frac{\partial}{\partial r} (r \sigma_{r\theta}) \\ & + \frac{\partial}{\partial z} \sigma_{\theta z} + \sigma_{r\theta} / r - \frac{1}{r} \frac{\partial}{\partial r} (r \overline{\rho' v' \bar{u}}) - \overline{\rho' u'} \frac{\partial}{\partial r} \bar{v} - \frac{\partial}{\partial z} (\overline{\rho' v' \bar{w}}) \\ & - \overline{\rho' w'} \frac{\partial}{\partial z} \bar{v} - \overline{\rho' v' \bar{u}} / r \pm [\bar{\rho}_p (\bar{v}_p - \bar{v}_g) + \overline{\rho'_p v'_p} - \overline{\rho'_p v'_g}] / t_s. \end{aligned} \quad (\text{A12})$$

In contrast, experience also showed that the vertical momentum equation was most stable in conservative form. Reynolds averaging Eq. (A4) directly then gives

$$\begin{aligned} \frac{\partial}{\partial t} (\bar{\rho} \bar{w}) + \frac{\partial}{\partial t} \overline{\rho' w'} + \frac{1}{r} \frac{\partial}{\partial r} (r \bar{\rho} \bar{u} \bar{w}) + \frac{\partial}{\partial z} (\bar{\rho} \bar{w}^2) = & -\frac{\partial}{\partial z} \bar{P} - \bar{\rho} G M z / R^3 \\ & + \frac{1}{r} \frac{\partial}{\partial r} (r \sigma_{rz}) + \frac{\partial}{\partial z} \sigma_{zz} - \frac{1}{r} \frac{\partial}{\partial r} (r \overline{\rho' u' \bar{w}}) - \frac{1}{r} \frac{\partial}{\partial r} (r \overline{\rho' w' \bar{u}}) \\ & - 2 \frac{\partial}{\partial z} (\overline{\rho' w' \bar{w}}) \pm [\bar{\rho}_p (\bar{w}_p - \bar{w}_g) + \overline{\rho'_p w'_p} - \overline{\rho'_p w'_g}] / t_s. \end{aligned} \quad (\text{A13})$$

Here we have defined the turbulent Reynolds stresses

$$\begin{aligned} \sigma_{rr} &= -\overline{\rho' u' u'} - \overline{\rho' u' u'}, & \sigma_{\theta z} &= -\overline{\rho' v' w'} - \overline{\rho' v' w'}, \\ \sigma_{\theta\theta} &= -\overline{\rho' v' v'} - \overline{\rho' v' v'}, & \sigma_{rz} &= -\overline{\rho' u' w'} - \overline{\rho' u' w'}, \\ \sigma_{zz} &= -\overline{\rho' w' w'} - \overline{\rho' w' w'}, & \sigma_{r\theta} &= -\overline{\rho' u' v'} - \overline{\rho' u' v'} \end{aligned} \quad (\text{A14})$$

for both phases.

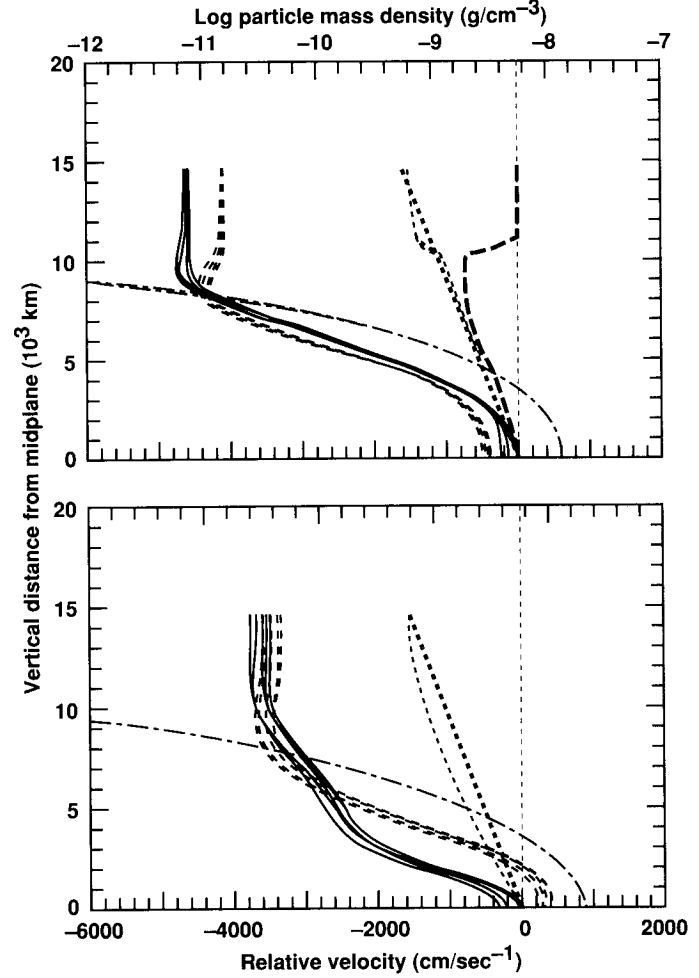


FIG. A1. Comparison of particle velocities obtained using Reynolds (top) and Favre (bottom) averaging. The particle radial, longitudinal, and vertical velocities are u_p , v_p , and w_p , respectively. Particle velocities are shown relative to Keplerian velocity v_K (Section 1.1.1, Section 3, and Weidenschilling 1977). The particle mass density profile is the dot-dashed line (mass density scale along the top axis). Drag coefficients were slightly different in the two cases, accounting for the different velocities high above the turbulent boundary layer. Drag coefficients in this comparison also differ from those employed in the remainder of the paper: for example, in these two cases the Schmidt number is calculated using the orbital frequency for the eddy turnover frequency, which somewhat increases the diffusivity of the particles. Nevertheless, these two cases illustrate the relative differences between Favre- and Reynolds-averaged results. Note in the Favre solution that there is no change in the particle fall velocity in the turbulent boundary layer, whereas one would expect turbulent diffusion to diminish it. This is partly an issue of inconsistent definitions. Furthermore, note the fact that the particle longitudinal velocities v_p exceed Keplerian near the midplane, apparently a nonphysical result. In other cases using Favre averaging we have seen the particles acquire an outward drift velocity near the midplane, also, we believe, nonphysical. Both of these difficulties are cured in the Reynolds-averaged solution (top).

It remains to model the correlations appearing in (A7) and (A11)–(A14) above. Equation (B8) of Appendix B implies that the terms of the form $\overline{\rho'_p u'_p} - \overline{\rho'_p u'_g}$ nearly cancel out of Eqs. (A11)–(A13). Presuming $\overline{\rho'_p} \ll \bar{\rho}$ enables us also to neglect the triple correlations of the form $\overline{\rho' u' v'}$ in

Eqs. (14). Note, however, that direct numerical simulations of turbulence in a two-phase fluid (Squires and Eaton 1990, 1991a,b) show large fluctuations in ρ_p which may invalidate this last approximation under some circumstances.

APPENDIX B: PARTICLE DIFFUSION

When Eqs. (A11)–(A14) of Appendix A are applied to the particle phase, we require correlations of the form $\overline{u'_p u'_p}$, $\overline{u'_p v'_p}$, etc. between the particle velocity components. These correlations may be interpreted as particle momentum fluxes, analogous to the Reynolds stresses in the gaseous phase. In fact, it proves most useful to express them in terms of the gas velocity correlations.

Since the fluctuating forces on the particles are dominated by gas drag, the governing equation for their velocity variations may be written

$$\frac{\partial}{\partial t} u'_p = (u'_g - u'_p)/t_s \quad (\text{B1})$$

and analogous equations for the other two components v'_p and w'_p . To solve these, we Fourier analyze the velocity fluctuations into terms of the form

$$\begin{aligned} u'_g(t) &= \int_0^\infty [A(\omega)e^{i\omega t} + A^*(\omega)e^{-i\omega t}] d\omega, \\ u'_p(t) &= \int_0^\infty [B(\omega)e^{i\omega t} + B^*(\omega)e^{-i\omega t}] d\omega, \end{aligned} \quad (\text{B2})$$

where A and B are complex amplitudes, ω is an angular frequency, i is the imaginary unit, and the asterisk denotes the complex conjugate. Analogous relations hold for the v and w components. Then (B1) above implies

$$\begin{aligned} i\omega B &= (A - B)/t_s \Rightarrow B = A/(1 + i\omega t_s), \\ i\omega B^* &= (A^* - B^*)/t_s \Rightarrow B^* = A^*/(1 - i\omega t_s) \end{aligned} \quad (\text{B3})$$

for each frequency.

Since different frequencies are orthogonal, the correlations immediately become

$$\overline{u'_g u'_g} = 2A^* A, \quad (\text{B4})$$

$$\overline{u'_p u'_g} = A^* B + B^* A = 2A^* A/(1 + \omega^2 t_s^2), \quad (\text{B5})$$

$$\overline{u'_p u'_p} = 2B^* B = 2A^* A/(1 + \omega^2 t_s^2), \quad (\text{B6})$$

and similarly for v and w . In terms of the gas correlation $\overline{u'_g u'_g}$, Eqs. (B5) and (B6) above give

$$\overline{u'_p u'_g} = \overline{u'_p u'_p} = \overline{u'_g u'_g}/(1 + \omega^2 t_s^2). \quad (\text{B7})$$

Note that the rms fluctuation $\sqrt{\overline{u'_p u'_p}}$ in u'_p is less than $\sqrt{\overline{u'_g u'_g}}$, that in u'_g , by a factor of $1/\sqrt{1 + \omega^2 t_s^2}$. Note also the interesting fact that the phase lag between the gas forcing and the particle response induces a correlation coefficient between u'_p and u'_g of the same factor, so that $\overline{u'_p u'_g} = \overline{u'_p u'_p}$. Similarly, analysis of the correlations between different components gives

$$\overline{u'_p v'_g} \approx \overline{u'_p v'_p} = \overline{u'_g v'_g}/(1 + \omega^2 t_s^2) \quad (\text{B8})$$

and analogous results.

Equations (B3)–(B9) above describe the response of the particles to gas eddies of a single frequency, but the particles are subject to a whole range of eddies and couple most efficiently to those with the lowest frequencies. The distribution of frequencies in isotropic turbulence can be described by the turbulent energy spectrum $E(\omega)$, where

$$\overline{u'_g u'_g} = \overline{v'_g v'_g} = \overline{w'_g w'_g} = \frac{2}{3} k = \frac{2}{3} \int_0^\infty E(\omega) d\omega. \quad (\text{B9})$$

(The upper limit really extends to the Kolmogorov frequency, but the difference is negligible.) Meek and Jones (1973) give

$$E(\omega) \approx \frac{2}{\pi} k Y / (1 + Y^2 \omega^2), \quad (\text{B10})$$

where Y is called the “integral time scale.” When averaged over this spectrum, Eqs. (B8) and (B9) give

$$\begin{aligned} \overline{u'_p v'_g} / \overline{u'_g v'_g} &\approx \overline{u'_p v'_p} / \overline{u'_g v'_g} = \overline{u'_p u'_g} / \overline{u'_g u'_g} = \overline{u'_p u'_p} / \overline{u'_g u'_g} \\ &= k^{-1} \int_0^\infty E(\omega) d\omega / (1 + \omega^2 t_s^2) \\ &= \frac{2}{\pi} \int_0^\infty Y d\omega / (1 + Y^2 \omega^2) (1 + \omega^2 t_s^2) = (1 + t_s/Y)^{-1}, \end{aligned} \quad (\text{B11})$$

and analogous results for the other components. Results similar to (B11) above were obtained by Völk *et al.* (1980) by numerical integration over a wavenumber spectrum.

Particles falling through a gravitational field actually pass through different eddies more quickly than indicated above, due to their additional vertical velocity. To account for this “crossing-trajectories” effect, the right-hand sides of Eq. (B11) above should be divided by an additional factor,

$$\sqrt{1 + \overline{w_p^2} / \overline{w_p^2} / \overline{w_p^2}} = \sqrt{1 + 3\overline{w_p^2} / 2k} \quad (\text{B12})$$

(Csanady 1963).

Next consider the correlations $\overline{\rho'_p u'_p}$, $\overline{\rho'_p v'_p}$, and $\overline{\rho'_p w'_p}$ between particle density and velocity fluctuations appearing in Eqs. (A7) and (A11)–(A13) of Appendix A. These can be interpreted as mean mass fluxes driven by turbulent mixing. It is common to model such fluxes as proportional to the gradient of the mean particle density, by analogy to the molecular diffusion of heat or momentum. In our case, this “gradient diffusion hypothesis” (GDH) implies

$$\overline{\rho'_p u'_p} = -D \frac{\partial}{\partial r} \overline{\rho_p}, \quad \overline{\rho'_p v'_p} = -D/r \frac{\partial}{\partial \theta} \overline{\rho_p} = 0, \quad \overline{\rho'_p w'_p} = -D \frac{\partial}{\partial z} \overline{\rho_p}, \quad (\text{B13})$$

where D is the diffusivity of the particles. Again by a Reynolds-type analogy, D is taken as proportional to the eddy viscosity ν_t ,

$$D = \nu_t / \text{Sc}, \quad (\text{B14})$$

where the dimensionless constant of proportionality Sc is known as the Schmidt number (an analogue of the Prandtl number for thermal

diffusion). Typically, Sc is taken as $2k/(\overline{u_p'u_p'} + \overline{v_p'v_p'} + \overline{w_p'w_p'})$. Then Eqs. (B11) and (B12) above imply

$$Sc = (1 + t_s/Y)\sqrt{1 + 3\overline{w_p'^2}/2k}. \quad (B15)$$

APPENDIX C: LIST OF SYMBOLS

Parameter	Definition
C_D	Drag coefficient (Eqs. (46)–(48))
c	Gas molecule thermal speed
c_k	Pressure tensor scaling coefficient (Eq. (30))
c_L	Generic length scaling coefficient
c_p	Nebula gas specific heat at constant pressure (Eq. (29))
c_p	Particle random velocity
c_δ	1% boundary layer thickness scaling coefficient (Eq. (20))
c_μ	Kolmogorov–Prandtl coefficient (Eq. (32))
c_ν	Prandtl viscosity model coefficient (Eq. (23))
Δr_{acc}	radial range traversed by particles prior to accretion (Section 5.4)
ΔV	Velocity difference across boundary layer = $v_K - v_0$ (Section 2.2.1)
ΔV_g	Velocity difference between Keplerian planetesimal and embedded midplane gas
ΔV_p	Velocity difference between Keplerian planetesimal and drifting particle layer
δ	1% lengthscale
ε	Dissipation rate of turbulent kinetic energy k (Eqs. (31)–(33))
η	Pressure gradient force perturbation parameter (Eqs. (8), (59))
f	Ratio of turbulent velocity to overall shear velocity (Eq. (35))
f_G	Gravitational focussing factor for accretion (Section 5.4)
F_{acc}	Mass fraction of drifting particles accreted onto planetesimals (Section 5.4)
G	Universal gravitation constant = 6.7×10^{-8} cgs
H_p	Particle layer thickness (Section 1)
k	Turbulent kinetic energy per unit gas mass density (Eq. (30))
L	Generic length scale
L_E	Ekman lengthscale (Eq. (20))
l	Turbulent mixing length in boundary layer (Section 2.2)
λ	Gas molecular mean free path
M_\odot	Solar mass = 2×10^{33} g
μ_T	Turbulent dynamic viscosity = $\rho_g \nu_T$
ν_m	Molecular kinematic viscosity $\sim 10^5$ cm ² sec ^{−1}
ν_T	Turbulent kinematic viscosity (Eqs. (19), (21), (24), (26))
Ω	Orbital frequency $\approx 2.1 \times 10^{-7}$ (r/1 AU) ^{−3/2}
Ω_c	Large eddy turnover frequency (Eq. (34))
ω	Vorticity (Eq. (33))
P	Gas pressure
p	Nebula surface mass density radial powerlaw dependence (3/2; Section 3)
q	Nebula photosphere temperature radial powerlaw dependence (1/2; Section 3)
R_g	Universal gas constant = 8.31×10^7 cgs (Section 3)
Re	Flow Reynolds number
Re^*	Critical Reynolds number (Eq. (19))
Re_p	Particle Reynolds number (Eq. (46))
Ri	Richardson number (Eq. (29))
Ro	Rossby number (Eq. (25))
r	Radial coordinate

Parameter	Definition
r_0	Reference radius for nebula physical model (1 AU; Section 3)
r_p	Planetesimal radius
r_p	Particle radius
ρ^*	Roche density (Section 1)
ρ_g	Gas volume mass density near midplane (Section 3)
$\bar{\rho}_p, \rho'_p$	Mean and fluctuating particle layer volume mass density
$\rho_{p,crit}$	Critical value of ρ_p for gravitational instability (Section 1)
$\rho_{p,min}$	Numerical lower limit on ρ_p (Section 2.4)
ρ_s	“Solid” internal density of a particle (Section 2.3.1)
Sc	Schmidt number (Eqs. (40) and (B15))
St	Stokes number (Eq. (41))
σ_0	Nebula total surface mass density at reference location (Section 3)
σ_p	Particle layer surface mass density (Section 1)
t_d	Radial drift time of particle due to gas drag (Eqs. (65)–(66))
t_s	Stopping time of particle due to gas drag (Eqs. (49)–(51))
$t_{m,b}$	Mass growth time due to binary gravitational encounters
$t_{m,d}$	Mass growth time due to differential drift effects
T_0	Nebula temperature at reference location (280 K; Section 3)
τ_p	Planetesimal ensemble optical depth (Section 5.4)
τ_p	Particle layer optical depth (Section 5.5)
θ	Angular coordinate
U, V	Generic velocity scales
u_p	Planetesimal radial drift velocity (Section 5.4)
\bar{u}_g, u'_g	Mean and fluctuating gas radial velocity
\bar{u}_p, u'_p	Mean and fluctuating particle radial velocity
\bar{v}_g, v'_g	Mean and fluctuating gas azimuthal velocity
\bar{v}_p, v'_p	Mean and fluctuating particle azimuthal velocity
v_0	Pressure stabilized gas rotation velocity (Eq. (7))
v_K	Keplerian orbital velocity
w_{diff}	Particle vertical “diffusion” velocity (Eq. (62))
w_F	Particle terminal vertical velocity (Eq. (61))
\bar{w}_p, w'_p	Mean and fluctuating particle vertical velocity
Y	Integral time scale of the turbulence (Eq. (41))
z	Vertical coordinate, from midplane

ACKNOWLEDGMENTS

We thank Tom Coakley of the Fluid Dynamics Division at Ames Research Center for his considerable input during the earliest stages of this work and for his thorough reading of the manuscript and helpful suggestions on improving it. We also thank Bill Cabot, Pat Cassen, Joel Ferziger, Bob Hogan, Peter Goldreich, Victor Safronov, Bill Skinner, Bill Ward, and Stu Weidenschilling for their valuable conversations and suggestions. J.N.C. thanks Alan Harris for mentioning over a decade ago that two-phase systems have intriguing and counterintuitive behavior, a suggestion which eventually led to this project. We thank our referees for their very thorough reviews, and constructive suggestions. This work was initiated using support from the Ames Director’s Discretionary Fund; we thank both NASA’s Planetary Geology and Geophysics Program and Origins of Solar Systems Program for all subsequent financial support. The numerical modeling would not have been possible without the capabilities provided by the NASA Office of Aeronautics National Aerodynamical Simulator Program, operated at Ames Research Center.

REFERENCES

- ADACHI, I., C. HAYASHI, AND K. NAKAZAWA 1976. The gas drag effect on the elliptical motion of a solid body in the primordial solar nebula. *Prog. Theor. Phys.* **56**, 1756–1771.
- BARGE, P., AND R. PELLAT 1991. Mass spectrum and velocity dispersions during planetesimal accretion. *Astrophys. J.* **93**, 270–287.
- BATCHELOR, G. K. 1967. *An Introduction to Fluid Dynamics*. Cambridge University Press.
- BECKWITH, S., A. SARGENT, R. S. CHINI, AND R. GÜSTEN 1990. A survey for circumstellar disks around young stellar objects. *Astron. J.* **99**, 924–944.
- BECKWITH, S., AND A. SARGENT 1991. Particle emissivity in circumstellar disks. *Astrophys. J.* **381**, 250–258.
- BORDERIES, N., P. GOLDREICH, AND S. TREMAINE 1983. Perturbed particle disks. *Icarus* **55**, 124–132.
- BOSS, A. 1992. Thermal structure of the solar nebula. *Lunar Planet. Sci. Conf. XXIII*, 141–142.
- CABOT, W., V. M. CANUTO, O. HUBICKYJ, AND J. B. POLLACK 1987a. The role of turbulent convection in the primitive solar nebula. I. Theory. *Icarus* **69**, 387–422.
- CABOT, W., V. M. CANUTO, O. HUBICKYJ, AND J. B. POLLACK 1987b. The role of turbulent convection in the primitive solar nebula. II. Results. *Icarus* **69**, 423–457.
- CABOT, W., O. HUBICKYJ, J. B. POLLACK, AND P. CASSEN 1990. Direct numerical simulations of turbulent convection. I. Variable gravity and uniform rotation. *Geophys. Astrophys. Fluid Dynamics* **53**, 1–42.
- CABOT, W., AND J. B. POLLACK 1992. Direct numerical simulations of turbulent convection. II. Variable gravity and differential rotation. *Geophys. Astrophys. Fluid Dynamics* **55**, 97–133.
- CANUTO, V., AND R. BATTAGLIA 1988. Turbulent diffusivity. *Astron. Astrophys.* **193**, 313–326.
- CASSEN, P. M. 1992. Thermal models of the primitive solar nebula. *Lunar Planet. Sci. Conf. XXIII*, 207–208.
- CASSEN, P. M., F. H. SHU, AND S. TEREBY 1985. Protostellar disks and star formation: An overview. In *Protostars and Planets II* (D. Black and M. Matthews, Eds.), pp. 448–483. Univ. of Arizona Press, Tucson.
- CEBECI, T., AND A. M. D. SMITH 1974. *Analysis of turbulent boundary layers*. Academic Press, NY.
- CHAMPNEY, J. M., AND J. N. CUZZI 1990. *A Turbulent Two-Phase Flow Model for Nebula Flows*. Paper 90-0211, 28th AIAA Aerospace Sciences meeting, Reno, NV, January 1990.
- CHOKSHI, A., A. G. G. M. TIELENS, AND D. HOLLENBACH 1993. Dust coagulation. *Astrophys. J.* **407**, 806–819.
- COAKLEY, T. A. 1987. Unpublished lecture notes on turbulence modeling.
- COAKLEY, T. A., AND J. M. CHAMPNEY 1985. *Numerical simulation of compressible, turbulent, two-phase flow*. Paper 85-1666, AIAA Fluid Dynamics and Plasmadynamics conference, Cincinnati, OH, July 1985.
- COLEMAN, G. N., J. H. FERZIGER, AND P. R. SPALART 1990. A numerical study of the turbulent Ekman layer. *J. Fluid Mech.* **213**, 313–348.
- COLEMAN, G. N., J. H. FERZIGER, AND P. R. SPALART 1992. Direct simulation of the stably stratified turbulent Ekman layer. *J. Fluid Mech.* **244**, 677–712.
- CORADINI, A., C. FEDERICO, AND G. MAGNI 1981. Formation of planetesimals in an evolving protoplanetary disk. *Astron. Astrophys.* **98**, 173–185.
- CORADINI, A., G. MAGNI, AND A. C. FEDERICO 1980. Time evolution of grains in the protosolar nebula. *Moon Planets* **22**, 47–62.
- CROWE, C. T., R. A. GORE, AND T. R. TROUTT 1985. Particle dispersion by coherent structures in free shear flows. *Particulate Sci. Technol.* **3**, 149–158.
- CSANADY, G. T. 1963. Turbulent diffusion of heavy particles in the atmosphere. *J. Atmos. Sci.* **14**, 171–194.
- CUZZI, J. N., AND R. H. DURISEN 1990. Bombardment of planetary rings by meteoroids; general formulation and effects of Oort cloud projectiles. *Icarus* **84**, 467–501.
- CUZZI, J. N., AND S. J. WEIDENSCHILLING 1992. *Grain Growth and Nebula Opacity*. Presented at Conference on Disk Dispersal, Institute of Theoretical Physics, University of California, Santa Barbara, August 1992.
- CUZZI, J. N., J. M. CHAMPNEY, T. A. COAKLEY, AND A. R. DOBROVOLSKIS 1989. Particle-gas dynamics in the protoplanetary nebula. *Lunar Planet. Sci. Conf. XX*, 216–217. [Abstracts]
- DOBROVOLSKIS, A. R. 1983. Atmospheric Tides on Venus. III. The planetary boundary layer. *Icarus* **56**, 165–175.
- EDGEWORTH, K. E. 1949. The origin and evolution of the Solar System. *Mon. Not. R. Acad. Sci.* **109**, 600–609.
- ELMEGREEN, B. G. 1978. On the interaction between a strong stellar wind and a surrounding disk nebula. *Moon Planets* **19**, 261–279.
- ELMEGREEN, B. G. 1979. On the disruption of a protoplanetary disk nebula by a T Tauri like solar wind. *Astron. Astrophys.* **80**, 77.
- GOLDREICH, P., AND W. R. WARD 1973. The formation of planetesimals. *Astrophys. J.* **183**, 1051–1061.
- GRIMM, R. E., AND H. MCSWEEN 1993. Heliocentric zoning of the asteroid belt by 26-Al heating. *Science* **259**, 653–655.
- HAACK, H., K. RASMUSSEN, AND P. H. WARREN 1990. Effects of regolith/megaregolith insulation on the cooling histories of differentiated asteroids. *J. Geophys. Res.* **95**, 5111–5124.
- HARTMANN, L., S. KENYON, AND P. HARTIGAN 1993. Young stars: Episodic phenomena, activity, and variability. In *Protostars and Planets III* (E. H. Levy and J. Lunine, Eds.). Univ. of Arizona Press, Tucson.
- HAYASHI C. 1981. Structure of the solar nebula, growth and decay of magnetic fields, and effects of magnetic and turbulent viscosities on the nebula. *Progr. Theor. Phys. Suppl.* **70**, 35–53.
- HINZE, J. O. 1975. *Turbulence*, 2nd ed. McGraw-Hill, New York.
- HOLTON, J. R. 1972. *An Introduction to Dynamic Meteorology*. Academic Press, New York.
- KENNARD, E. H. 1938. *Kinetic Theory of Gases*. McGraw-Hill, New York.
- KOLVOORD, R. A., AND R. GREENBERG 1992. A critical reanalysis of planetary accretion models. *Icarus* **98**, 2–19.
- LIN, D. N. C., AND J. PAPALOIZOU 1980. On the structure and evolution of the primordial solar nebula. *Mon. Not. R. Ast. Soc.* **191**, 37–48.
- LIN, D. N. C., AND J. PAPALOIZOU 1985. On the dynamical origin of the solar system. In *Protostars and Planets II* (D. Black and M. Matthews, Eds.), pp. 981–1072. Univ. of Arizona Press, Tucson.
- LISSAUER, J. J. 1987. Timescales for planetary accretion and the structure of the protoplanetary disk. *Icarus* **69**, 249–265.
- MACCORMACK, R. W. 1969. The effect of viscosity in hypervelocity impact cratering. AIAA paper 69–354. AIAA, New York.
- MEEK, C. C., AND B. G. JONES 1973. Studies of the behavior of heavy particles in a turbulent fluid flow. *J. Atmos. Sci.* **30**, 239–244.
- MIYAKE, K., AND Y. NAKAGAWA 1992. *Effects of Grain Growth on Spectral Energy Distribution of Protoplanetary Nebulae*. Presented at Conference on Disk Dispersal, Institute of Theoretical Physics, University of California, Santa Barbara, August 1992.

- MIYAKE, K., AND Y. NAKAGAWA 1993. Effects of particle growth on opacity curves of protoplanetary disks around T Tauri stars. Submitted for publication.
- MIZUNO, H., K. NAKAZAWA, AND C. HAYASHI 1978. Instability of gaseous envelope surrounding planetary core and formation of giant planets. *Prog. Theor. Phys.* **64**, 699–710.
- MIZUNO, H., W. J. MARKIEWICZ, AND H. J. VÖLK 1988. Grain growth in turbulent protoplanetary accretion disks. *Astron. Astrophys.* **195**, 183–192.
- MORFILL, G. E., AND H. J. VÖLK 1984. Transport of dust, vapor, and chemical fractionation in the early protosolar cloud. *Astrophys. J.* **287**, 371–395.
- NAKAGAWA, Y., M. SEKIYA, AND C. HAYASHI 1986. Settling and growth of particles in a laminar phase of a low-mass solar nebula. *Icarus* **67**, 375–390.
- NAKAGAWA, Y., C. HAYASHI, AND K. NAKAZAWA 1983. Accumulation of planetesimals in the solar nebula. *Icarus* **54**, 361–376.
- PODOSEK, F. A., AND T. D. SWINDLE 1988. Extinct Radionuclides. In *Meteorites and the Early Solar System* (J. F. Kerridge and M. S. Matthews, Eds.), pp. 1093–1113. Univ. of Arizona Press.
- POLLACK, J. B., C. P. MCKAY, AND B. CHRISTOFFERSON 1985. A calculation of the Rosseland mean opacity of dust grains in primordial solar system nebulae. *Icarus* **64**, 471–492.
- PRINN, R. G. 1990. On neglect of nonlinear momentum terms in solar nebula accretion disk models. *Astrophys. J.* **348**, 725–729.
- ROCARD, Y. 1952. *Thermodynamique*. Masson, Paris.
- RODI, W. 1980. Turbulence models and their applications. In *Hydraulics—A State of the Art Review*. International Association for Hydraulic Research, Delft, The Netherlands.
- RUDEN, S., AND D. N. C. LIN 1986. The global evolution of the primordial solar nebula. *Astrophys. J.* **308**, 883.
- RUDEN, S., AND J. B. POLLACK 1991. The dynamical evolution of the protosolar nebula. *Astrophys. J.* **375**, 740–760.
- RUFF, G. A., AND G. M. FAETH 1987. Dense-Spray structure and phenomena. Part II. Pressure-Atomized Sprays. AFOSR-TR-87-2009 Interim Report July '86–July '87.
- SAFRONOV, V. S. 1969. *Evolution of the Protoplanetary Cloud and the Formation of the Earth and Planets*. NASA TTF-677.
- SAFRONOV, V. S. 1987. Evolution of the dust component of the circum-solar protoplanetary disk. *Astron. Vestnik* **XXI**, 216–220. [in Russian]
- SAFRONOV, V. S. 1991. Kuiper prize lecture: Some problems in the formation of the planets. *Icarus* **94**, 260–271.
- SAFRONOV, V. S. 1992. *Gravitational Instabilities in Disks*. Presented at Workshop on Planetesimal Formation, Institute of Theoretical Physics, University of California, Santa Barbara, December 1992.
- SCHLICHTING, H. 1969. *Boundary Layer Theory*. McGraw-Hill, New York.
- SEKIYA, M. 1983. Gravitational Instabilities in a dust-gas layer and formation of planetesimals in the solar nebula. *Prog. Theor. Phys.* **69**, 1116–1130.
- SEKIYA, M., AND Y. NAKAGAWA 1988. Settling of dust particles and formation of planetesimals. *Prog. Theor. Phys. Suppl.* **96**, 141–150.
- SHU, F. H., C. YUAN, AND J. J. LISSAUER 1985. Nonlinear spiral density waves: An inviscid theory. *Astrophys. J.* **291**, 356–376.
- SPROULL, W. T. 1961. Viscosity of dusty gases. *Nature* **190**, 976–978.
- SQUIRES, K. D., AND J. K. EATON 1990. Particle response and turbulence modification in isotropic turbulence. *Phys. Fluids* **A2**, 1191–1203.
- SQUIRES, K. D., AND J. K. EATON 1991a. Preferential concentration of particles by turbulence. *Phys. Fluids* **A3**, 1169–1178.
- SQUIRES, K. D., AND J. K. EATON 1991b. Measurements of particle dispersion obtained from direct numerical simulations of isotropic turbulence. *J. Fluid Mech.* **226**, 1–35.
- STEVENSON, D. J., AND J. LUMINE 1988. Rapid formation of Jupiter by diffusive redistribution of water vapor in the solar nebula. *Icarus* **75**, 146.
- SUSSMAN, M. A., AND G. J. WILSON 1991. *Computation of Chemically Reacting Flow Using a Logarithmic Form of the Species Conservation Equations*. Proceedings of the Fourth International Symposium on Computational Fluid Dynamics, Vol. II, University of California, Davis.
- SWINDLE, T. D., AND F. A. PODOSEK 1988. Iodine–Xenon dating. In *Meteorites and the Early Solar System*. (J. F. Kerridge and M. S. Matthews, Eds.). Univ. of Arizona Press, Tucson.
- TENNEKES, H., AND J. L. LUMLEY 1972. *A First Course in Turbulence*. MIT Press, Cambridge, MA.
- TOOMRE, A. J. 1964. On the gravitational stability of a disk of stars. *Astrophys. J.* **139**, 1217–1238.
- VÖLK, H. J., F. C. JONES, G. E. MORFILL, AND S. RÖSER 1980. Collisions between grains in a turbulent gas. *Astron. Astrophys.* **85**, 316–325.
- WASSON, J. T., AND G. W. KALLEMEYN 1988. Compositions of chondrites. *Phil. Trans. R. Soc. Lond. A*, **325**, 535–544.
- WATANABE, S. I., AND MIYAMA, S. M. 1992. Collision and tidal interaction between planetesimals. *Astrophys. J.* **391**, 318–335.
- WEIDENSCHILLING, S. J. 1977. Aerodynamics of solid bodies in the solar nebula. *Mon. Not. R. Acad. Soc.* **180**, 57–70.
- WEIDENSCHILLING, S. J. 1980. Dust to planetesimals: Settling and coagulation in the solar nebula. *Icarus* **44**, 172–189.
- WEIDENSCHILLING, S. J. 1984. Evolution of grains in a turbulent solar nebula. *Icarus* **60**, 555–567.
- WEIDENSCHILLING, S. J. 1988. Formation processes and timescales for meteorite parent bodies. In *Meteorites and the Early Solar System* (J. F. Kerridge and M. S. Matthews, Eds.). Univ. of Arizona Press, Tucson.
- WEIDENSCHILLING, S. J., AND J. N. CUZZI 1993. Formation of planetesimals in the solar nebula. In *Protostars and Planets III*, (E. H. Levy and J. L. Lunine, Eds.). University of Arizona Press, Tucson.
- WEIDENSCHILLING, S. J., B. DONN, AND P. MEAKIN 1989. Physics of planetesimal formation. In *The Formation and Evolution of Planetary Systems* (H. A. Weaver and L. Danly, eds.). Cambridge Univ. Press.
- WETHERILL, G. W. 1980. Formation of the terrestrial planets. *Ann. Rev. Astron. Astrophys.* **18**, 77–113.
- WETHERILL, G. W. 1990. Formation of the Earth. *Ann. Revs. Earth Planet. Sci.* **18**, 205–256.
- WHIPPLE, F. L. 1972. On certain aerodynamic processes for asteroids and comets. In *From Plasma to Planet* Proceedings of the Nobel Symposium 21 (A. Elvius, Ed.). Wiley, New York.